



# A numerical study of super-resolution through fast 3D wideband algorithm for scattering in highly-heterogeneous media<sup>☆</sup>



Pierre-David Létourneau<sup>a,\*</sup>, Ying Wu<sup>b</sup>, George Papanicolaou<sup>c</sup>,  
Josselin Garnier<sup>d</sup>, Eric Darve<sup>e,f</sup>

<sup>a</sup> Reservoir Labs, New York City, NY, United States

<sup>b</sup> Division of Computer, Electrical and Mathematical Science and Engineering, King Abdullah University of Science and Technology, Thuwal, 23955-2900, Saudi Arabia

<sup>c</sup> Department of Mathematics, Stanford University, United States

<sup>d</sup> Laboratoire de Probabilités et Modèles Aléatoires, Université Paris Diderot, France

<sup>e</sup> Institute for Computational and Mathematical Engineering, Stanford University, United States

<sup>f</sup> Mechanical Engineering Department, Stanford University, CA, United States

## HIGHLIGHTS

- Waves in random media.
- Numerical methods for waves.
- Fast multipole method.
- Super-resolution.
- Meta-material.

## ARTICLE INFO

### Article history:

Received 1 May 2016

Received in revised form 22 August 2016

Accepted 27 August 2016

Available online 19 September 2016

### Keywords:

Fast multipole method

Multiple scattering

Waves in inhomogeneous media

Super-resolution

Homogenization

## ABSTRACT

We present a wideband fast algorithm capable of accurately computing the full numerical solution of the problem of acoustic scattering of waves by multiple finite-sized bodies such as spherical scatterers in three dimensions. By full solution, we mean that no assumption (e.g. Rayleigh scattering, geometrical optics, weak scattering, Born single scattering, etc.) is necessary regarding the properties of the scatterers, their distribution or the background medium. The algorithm is also fast in the sense that it scales linearly with the number of unknowns. We use this algorithm to study the phenomenon of super-resolution in time-reversal refocusing in highly-scattering media recently observed experimentally (Lemoult et al., 2011), and provide numerical arguments towards the fact that such a phenomenon can be explained through a homogenization theory.

© 2016 Elsevier B.V. All rights reserved.

<sup>☆</sup> The work described here were partially supported by King Abdullah University of Science and Technology and the Army High Performance Computing Research Center (AHPCRC) (sponsored by the U.S. Army Research Laboratory under contract No. W911NF-07-2-0027) at Stanford University.

\* Corresponding author.

E-mail address: [letourneau@reservoir.com](mailto:letourneau@reservoir.com) (P.-D. Létourneau).

## 1. Introduction

In the past few decades, theory has been developed that demonstrates the vast array of physical phenomena, and the immense technical potential offered by highly heterogeneous three-dimensional media constituted by a large number of scatterers embedded in a background medium. Examples include subwavelength imaging [1–4], filtering and beam shaping [5] as well as cloaking [6] to name but a few. Some of these ideas have been verified experimentally with positive results [3,4,7,8]. Computational results on the other hand appear to be scarcer. The reason for this lies in the high computational cost associated with the solution of such problems, especially in three dimensions.

Following these observations, we present here work that is two-fold in its goal: in a first time, we introduce an algorithm capable of efficiently tackling the problem of simulating the propagation of waves in highly-heterogeneous media. Then, we use this algorithm to numerically study the problem of super-resolution in time-reversal refocusing in strongly scattering media.

Time reversal of waves was extensively investigated in the last twenty years [9–13]. A time-reversal mirror is a set of transducers that can be used as receivers or as transmitters. A typical time-reversal experiment has two steps. In the first step, a point-like source generates a wave that propagates through a medium and is recorded by the time-reversal mirror used as a set of receivers. In the second step, the time-reversal mirror is used as an array of transmitters, it re-emits the time-reversed recorded signals. It can then be observed that the wave focuses back at the initial source location. The refocusing properties have been studied experimentally, numerically, and theoretically. They are characterized by diffraction-limited focal spots, that is to say, the size of the time-reversed focal spot is of the order of the source central wavelength. In more detail, when the time-reversal mirror has full aperture, i.e. it completely surrounds the original source, the focal spot has the form of the imaginary part of the Green's function, which is a sinc function with a radius equal to half a wavelength when the medium is homogeneous and three-dimensional. This is the so-called diffraction limit [14]. When the time-reversal mirror has finite size, then the size of the focal spot is given by the Rayleigh resolution formula that depends on the wavelength and the aperture of the mirror [15].

Enhanced refocusing is a property observed in many time-reversal experiments. First, if we consider limited-aperture time-reversal mirrors, then it is possible to exploit the scattering properties of the medium to beat the Rayleigh resolution formula, but without overcoming the diffraction limit. Indeed multiple scattering due to random inhomogeneities in the medium can increase the directional diversity of waves, which increases the effective aperture and enhances time-reversal refocusing [16–21]. If we consider the case of a full-aperture time-reversal mirror, then the focal spot is expected to be diffraction-limited, with a focal spot radius equal to half the central wavelength. However, several mechanisms could be responsible for super-resolution, that is to say, time-reversal refocusing beyond the diffraction limit. First, the diffraction limit can be overcome if the source is replaced by its time-reversed analogue during the second step of the time-reversal experiment. This requires the use of an active sink that absorbs the time-reversed wave precisely at the original source location and at the refocusing time [22]. Second it is possible to obtain subwavelength focusing when the initial source is in the near field of the time-reversal mirror [23]. Third, focusing beyond the diffraction limit with far field time reversal is possible, provided a random distribution of small and strong scatterers is placed in the near field of the original source, as observed in the experiments reported in [24–27]. It was theoretically predicted that this apparent super-resolution effect could be explained by homogenization theory [28,29]. In our paper, we show by detailed numerical simulations using our algorithm that the apparent super-resolution phenomenon can indeed be explained by homogenization theory, i.e., the time-reversed focal spot can be described as a diffraction-limited focal spot obtained in an equivalent effective (or homogenized) medium that replaces the scattering medium. In other words, we show that the observed focal spot radius can be quantitatively explained by the classical resolution formula  $\lambda_{\text{effective}}/2$  where  $\lambda_{\text{effective}}$  is the central wavelength of the pulse computed in the effective medium computed by homogenization.

Our numerical algorithm is based on a T-matrix formulation [30–34] (also known as the Multiple Scattering (MS) method [35,36]), and amounts to solving a linear system of equations (known as the generalized Foldy–Lax self-consistent system [37]) which takes the form,

$$(I - TA)x = b \tag{1}$$

where  $I$  is the identity matrix,  $T$  is a sparse matrix and  $A$  is a dense matrix. The advantages of the T-matrix method over the other techniques lie in the following key points: the T-matrix ( $T$ ) is block diagonal and can be applied in a very fast manner, and the matrix  $A$ , although generally dense, can be applied in a fast manner as well through a generalization of the Fast Multipole Method (FMM, [38–42]). The computational gains thus achieved make this approach very competitive compared to other computational strategies.

As just mentioned, we shall make use of the FMM in order to accelerate the matrix–vector product ( $Ax$ ). As described in Section 2.4, we shall in fact use two variants of the FMM; one in the high-frequency (HF) regime and one in the low-frequency (LF) regime. Broadly speaking, such regimes correspond to a problem where scatterers are “far apart” and “close to one another” respectively. The structure to be employed is shown schematically in Fig. 1. Irregular expansions and regular expansions refer to the mathematical objects used to represent the field scattered, and incident onto, each of the scatterer respectively (Section 2.2.1). Such a hybrid structure is necessary in order to be able to tackle broadband problems, i.e. problems belonging to the HF or LF regime or both. This point is of particular importance as many interesting problems involve small scatterers with very strong contrast that are close to one another relative to the background wavelength

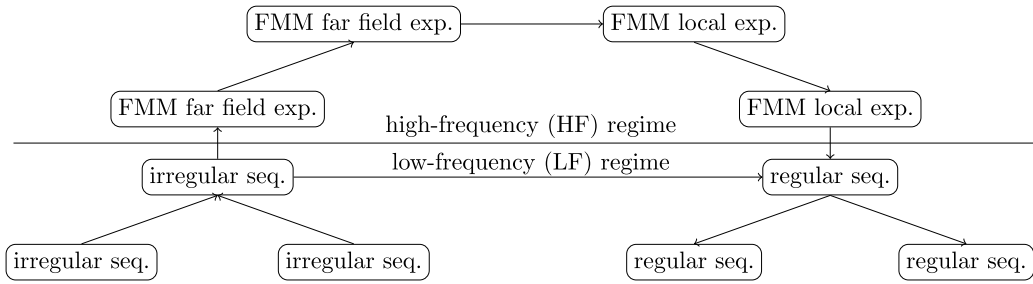


Fig. 1. Structure of fast hybrid code for the matrix–vector product  $Ax$ .

[35,43,25,44,45,24,3,4,7,8]. Such problem *cannot* be handled by the high-frequency variant of the FMM (HF-FMM) alone, for the latter exhibits a breakdown at low frequency. Moreover, they cannot be handled through naive dense matrix–vector product either as that would be too computationally expensive. The hybrid FMM therefore appears as the only means of approaching such problems.

Recent endeavors to tackle this issue using the T-matrix method are presented in Koc & Chew [33], Gumerov & Duraiswami [46], Hesford et. al [32] and Cheng et al. [30]. These however share many differences with the current algorithm in both their structure and their numerical analysis [47]; this work fills the gaps among all precursor methods in the sense that it can handle more general problems without suffering from computational instability, while possessing low computational complexity.

The paper is structured as follows: in Section 2 we provide a mathematical statement of the problem as well as a complete description of our algorithm. This includes mathematical preliminaries (Section 2.1), the Foldy–Lax multiple scattering formalism (Section 2.2), a complete description of the various theoretical tools (Section 2.3) as well as the computational framework (2.4). This is followed in Section 3 by a numerical study of super-resolution.

## 2. A fast algorithm for the propagation of acoustic waves in highly-scattering media

### 2.1. Preliminaries and notation

Throughout this paper, we shall let  $\mathbf{x} = (x_1, x_2, x_3) \in \mathbb{R}^3$  represent the Cartesian coordinates of a point in three-dimensional Euclidean space (3D). Boldface shall be used to represent vectors. We shall also make use of the Spherical coordinates which we designate by  $(r, \theta, \phi)$ . They are related to the Cartesian coordinates through the following relations,

$$\begin{aligned} x_1 &= r \sin(\theta) \cos(\phi) \\ x_2 &= r \sin(\theta) \sin(\phi) \\ x_3 &= r \cos(\theta) \end{aligned}$$

where  $\theta \in [0, \pi]$  and  $\phi \in [0, 2\pi]$ . The sphere of radius  $r$  centered at  $\mathbf{x}$  will be denoted as  $\mathcal{B}_r(\mathbf{x})$ . The absolute value  $|\mathbf{x}|$  or the absence of boldface  $(x)$  both represent the Euclidean norm and  $\hat{\mathbf{x}}$  denotes the unit vector in the direction of  $\mathbf{x}$ .

Given a function  $f(x_1, x_2, x_3)$  defined in  $[0, 1] \times [0, 1] \times [0, 1] \subset \mathbb{R}^3$ , we will write,

$$\mathcal{F}_{\mathbf{n}}[f] = \iiint_{[0,1]^3} f(x_1, x_2, x_3) e^{-2\pi i \sum_{i=1}^3 x_i \cdot n_i} dx_1 dx_2 dx_3$$

for the  $\mathbf{n}$ th Fourier coefficient of  $f(\cdot)$ . We denote the *spherical harmonics* of degree  $l$  and order  $m$  by,

$$Y_l^m(\theta, \phi) = \sqrt{\frac{2l+1}{4\pi} \frac{(l-m)!}{(l+m)!}} P_l^m(\cos(\theta)) e^{im\phi}$$

where  $l \in \mathbb{N}$  and  $|m| \leq l$ , and the functions  $P_l^m(\cdot)$  are the associated Legendre polynomials (8.6.6, 8.6.18, [48]),

$$P_l^m(x) = \frac{(-1)^m}{2^l l!} (1-x^2)^{m/2} \frac{d^{l+m}}{dx^{l+m}} (x^2-1)^l.$$

The spherical harmonics form a complete orthonormal system on  $L^2(\Omega)$  where  $\Omega$  represents the unit sphere in  $\mathbb{R}^3$  (Thm 2.7, [49]). Note that we included the Condon–Shortley phase  $((-1)^m)$  in the definition of the associated Legendre polynomials. We designate by  $j_l(z)$  and  $h_l^{(1)}(z)$  the spherical Bessel functions of the first kind and the spherical Hankel

functions of the first kind of order  $l$  respectively. They are defined as (10.1.1, [48]),

$$j_l(z) = \sqrt{\frac{\pi}{2z}} J_{l+1/2}(z)$$

$$h_l^{(1)}(z) = \sqrt{\frac{\pi}{2z}} (J_{l+1/2}(z) + iY_{l+1/2}(z))$$

for  $z \in \mathbb{C}$ , where  $J_{l+1/2}(z)$  and  $Y_{l+1/2}(z)$  are the half-order Bessel functions of the first and second kind respectively and  $i$  is the imaginary number, i.e.  $i^2 = -1$ . We shall call *regular spherical wave function* (RSWF) and *irregular spherical wave function* (ISWF) the quantities,

$$j_l(kr)Y_l^m(\theta, \phi)$$

$$h_l^{(1)}(kr)Y_l^m(\theta, \phi)$$

respectively, where  $k \in \mathbb{C}^+$  is the *wavenumber*. We shall designate by Spherical Wave Function (SWF) either of the above when the exact character is irrelevant. RSWF are entire/holomorphic solutions of Helmholtz equation in  $\mathbb{R}^3$ ,

$$(\Delta^2 + k^2) u = 0$$

whereas ISWF are radiating solutions of Helmholtz equation in  $\mathbb{R}^3 \setminus \{0\}$  (Thm 2.9, [49]). By radiating solution, we imply a solution of Helmholtz equation that satisfies Sommerfeld radiation conditions at infinity, i.e.,

$$\lim_{r \rightarrow \infty} r \left( \frac{\partial u}{\partial r} - iku \right) = 0. \tag{2}$$

Furthermore, ISWF can be used as a basis to expand radiating solutions of Helmholtz equation thanks to the following theorem (Thm 2.14, [49]),

**Theorem 1.** *Let  $u$  be a radiating solution to the Helmholtz equation in the exterior  $|x| > R > 0$  of a sphere. Then,  $u$  has an expansion with respect to spherical wave functions of the form,*

$$u(x) = \sum_{l=0}^{\infty} \sum_{m=-l}^l a_{l,m} h_l^{(1)}(k|x|)Y_l^m(\hat{\mathbf{x}})$$

that converges absolutely and uniformly on compact subsets of  $|x| > R$ . Conversely, if the above series converges in the mean square sense on the sphere  $|x| = R$  then it also converges absolutely and uniformly on compact subsets of  $|x| > R$  and  $u$  represents a radiating solution to the Helmholtz equation for  $|x| > R$ .

Series of the form,

$$\sum_{l=0}^{\infty} \sum_{m=-l}^l b_{l,m} j_l(k|x|)Y_l^m(\hat{\mathbf{x}}) \tag{3}$$

$$\sum_{l=0}^{\infty} \sum_{m=-l}^l a_{l,m} h_l^{(1)}(k|x|)Y_l^m(\hat{\mathbf{x}}) \tag{4}$$

will be referred to as *RSWF expansion* and *ISWF expansion* respectively, and the sequences  $\{b_{l,m}\}$  and  $\{a_{l,m}\}$  will be called *regular* and *irregular sequences* respectively. We will say that Eq. (3) is the expansion associated with the regular sequence  $\{b_{l,m}\}$  and that Eq. (4) is the expansion associated with the irregular sequence  $\{a_{l,m}\}$ .

## 2.2. Foldy–Lax formalism

We begin by introducing the problem we are interested in, that is the problem of time-harmonic acoustic scattering by multiple penetrable obstacles. We shall first describe it from a mathematical standpoint and then explain how it can be brought into a computational framework. For this purpose, we will introduce the T-matrix method which provides an explicit form for the solution operator of each scatterer in isolation, and will conclude with the Foldy–Lax formalism which, together with the T-matrix, gives rise to a self-consistent linear system amenable to a numerical solution.

### 2.2.1. Mathematical framework

Here, we present the problem in abstract mathematical terms. For this purpose, let  $\{\sigma_n\}_{n=1}^N \subset \mathbb{R}^3$ ,  $N \in \mathbb{N}$  be simply connected disjoint open subsets with  $C^2$  boundary contained in a ball of radius  $R < \infty$  centered at the origin. We shall refer to such regions as *scatterers*. Further, let  $k_0, \{k_n\}_{n=1}^N$  be some complex numbers with positive imaginary parts and  $\rho_0, \{\rho_n\}_{n=1}^N$  be some positive real numbers. Then, our problem consists in finding the solution of the following system of

**Table 1**  
Summary of relevant physical quantities.

Physical quantity	Symbol	Units	Relation
Frequency	$\omega$	Hz	
Density	$\rho$	kg/m <sup>3</sup>	
Bulk modulus	$\kappa$	Pa	
Speed of sound	$c$	m/s	$c = \sqrt{\kappa/\rho}$
Wavenumber	$k$	1/m	$k = 2\pi\omega/c$
Wavelength	$\lambda$	m	$\lambda = \frac{2\pi}{k}$

partial differential equations (PDEs),

$$\begin{aligned} (\Delta + k_0^2) u(\mathbf{x}) &= 0, & \forall \mathbf{x} \in \mathbb{R}^3 / \cup_{i=1}^N \sigma_n \\ (\Delta + k_n^2) u(\mathbf{x}) &= 0, & \forall \mathbf{x} \in \sigma_n \end{aligned}$$

where  $\Delta = \frac{\partial^2}{\partial x_1^2} + \frac{\partial^2}{\partial x_2^2} + \frac{\partial^2}{\partial x_3^2}$  is the Laplacian in 3-D. We further impose Sommerfeld radiation conditions at infinity (Eq. (2), Section 2.1), and transmission boundary conditions on each connected component of the boundary  $\partial\sigma_n$ ,

$$\begin{aligned} \lim_{\mathbf{x} \rightarrow \partial\sigma_n} u(\mathbf{x}) &= \lim_{\mathbf{x} \rightarrow \partial\sigma_n} u(\mathbf{x}) \\ \lim_{\mathbf{x} \rightarrow \partial\sigma_n} \hat{\mathbf{n}} \cdot \nabla u(\mathbf{x}) &= \frac{\rho_n}{\rho_0} \lim_{\mathbf{x} \rightarrow \partial\sigma_n} \hat{\mathbf{n}} \cdot \nabla u(\mathbf{x}) \end{aligned}$$

$\forall \mathbf{x} \in \partial\sigma_n$  where  $\hat{\mathbf{n}}$  represents the unit vector normal to the boundary and  $\nabla$  is the gradient. Furthermore,  $u(\mathbf{x})$  must take the form,

$$u(\mathbf{x}) = u^0(\mathbf{x}) + \tilde{u}(\mathbf{x})$$

where  $u^0(\mathbf{x})$  represents a known incident field satisfying the homogeneous Helmholtz with wave number  $k_0$  in all of  $\mathbb{R}^3$  except, possibly, at a discrete number of points in  $\mathbb{R}^3 / \cup_{i=1}^N \sigma_n$  (exterior source). Existence and uniqueness of the solution to this problem in the case where  $k_n = k'$  and  $\rho_n = \rho'$  for all  $n$ , and  $\rho_0, \rho', k_0, k' \in \mathbb{R}$  is guaranteed by [50]. This is the case where all scatterers have the same properties. Conditions under which existence and uniqueness is guaranteed for more general property distribution can be obtained from [51].

Finally, we have the following physical meaning for the parameters:  $k_0 = \frac{2\pi\omega}{c_0}$  and  $k_n = \frac{2\pi\omega}{c_n}$  are the wave numbers in the background medium and region  $\sigma_n$  respectively. Similarly,  $\lambda_0 = \frac{2\pi}{k_0}$  and  $\lambda_n = \frac{2\pi}{k_n}$  are the wavelengths in the background medium and region  $\sigma_n$ .  $2\pi\omega$  is the angular frequency, and  $c_0 = \sqrt{\frac{\kappa_0}{\rho_0}}$ ,  $c_n = \sqrt{\frac{\kappa_n}{\rho_n}}$  are the speed of sound in the background medium and region  $\sigma_n$  respectively.  $\kappa$  represents the bulk modulus and  $\rho$  refers to mass density. This is summarized in Table 1.

### 2.2.2. The T-matrix and the Foldy–Lax self-consistent linear system

The T-matrix is a name given to the explicit representation, under a given basis, of the solution operator for the (single scatterer) transmission problem as introduced in Section 2.2.1. Generally, spherical wave functions are used as a basis for this purpose. The method was first introduced by Waterman [34] and has been used and improved extensively since then (see [52] for a comprehensive database of T-matrix publications).

In the present context, the T-matrix has the following interpretation: consider a scatterer  $\sigma_n$  and let  $x_n \in \sigma_n$  be any point belonging to  $\sigma_n$ . We fix a coordinate system centered about  $x_n$  and refer to it as  $\sigma_n$ 's local coordinate system. Consider a RSWF expansion expressed in  $\sigma_n$ 's local coordinate and representing an incident field onto  $\sigma_n$  (Theorem 1, Section 2.1). Letting  $\mathbf{r} = \mathbf{x} - \mathbf{x}_n$  we have,

$$u_n^i(\mathbf{x}) = \sum_{l=0}^{\infty} \sum_{m=-l}^l b_{l,m} j_l(k_0 r) Y_l^m(\hat{\mathbf{r}}).$$

Furthermore, the field scattered by  $\sigma_n$  under this excitation can be represented through an ISWF expansion in  $\sigma_n$ 's local coordinates thanks to Theorem 1, Section 2.1. Thus, we write

$$u_n^s(\mathbf{x}) = \sum_{l=0}^{\infty} \sum_{m=-l}^l a_{l,m} h_l^{(1)}(k_0 r) Y_l^m(\hat{\mathbf{r}}). \tag{5}$$

The superscripts  $i$  and  $s$  stand for ‘‘incident’’ and ‘‘scattered’’ fields. The T-matrix is then the operator that takes the incident regular sequence  $\{b_{l,m}\}$  and transforms it into the scattered irregular sequence  $\{a_{l,m}\}$ . It is linear because Helmholtz equation is linear and exists thanks to results presented in Section 2.2.1. We thus have,

$$b = T a$$

where  $b$  and  $a$  are infinite sequences, and  $T$  is an infinite-dimensional matrix. All shall be truncated in due time for computational purposes.

Although the T-matrix method can be applied to scatterers of almost arbitrary shapes [34], we shall focus our attention to spherical scatterers in the present work. The consideration of more general shape can be integrated into the algorithm at a small cost if necessary, and spherical scatterers already produce rich enough phenomena for our purpose. In the particular case of spherical scatterers, the T-matrix takes a *diagonal* form, i.e. for  $\sigma_n$ , one has  $a_{l,m}^n = T_{(l,m)}^n b_{l,m}^n$ . Its entries are generally referred to as the Mie coefficients and are given explicitly by,

$$T_{(l,m)}^n = \frac{\gamma_n j_l(k_0 r_n) j_l'(k_n r_n) - j_l'(k_0 r_n) j_l(k_n r_n)}{h_l^{(1)'}(k_0 r_n) j_l(k_n r_n) - \gamma_n h_l^{(1)}(k_0 r_n) j_l'(k_n r_n)} \tag{6}$$

where  $\gamma_n = \frac{k_n \rho_0}{k_0 \rho_n}$ ,  $\prime$  stands for derivative w.r.t. the argument and  $r_n$  is the radius of the spherical scatterer  $\sigma_n$ . This is a classical result about which information can be found in [47] (Corollary 10, p.199) and [53,37,54]. We shall not repeat the details here.

The T-matrix provides a powerful analytical and computational tool to obtain the field scattered by a *single* scatterer. However, it does not provide for the interactions and the multiple scattering occurring when more than one scatterer are present. For this purpose, it is necessary to introduce the Foldy–Lax formalism (see e.g. [55,37]). The Foldy–Lax formalism for a system containing multiple scatterers consists in two main points: considering a particular scatterer, say  $\sigma_{n_0}$ , then,

- The field scatterer by  $\sigma_{n_0}$  is equal to its T-matrix ( $T^{n_0}$ ) applied to the total field impinging onto itself, i.e.,

$$u_{n_0}^s = T^{n_0} \cdot u_{n_0}^i.$$

- The total field impinging onto  $\sigma_{n_0}$  is equal to the sum of the external excitation ( $u^0$ ) and the field scattered by all other scatterers ( $u_n^s, n \neq n_0$ ), i.e.,

$$u_{n_0}^i = u^0 + \sum_{\substack{n=1 \\ n \neq n_0}}^N u_n^s.$$

In order to be able to apply a given scatterer’s T-matrix to an incident field however, the latter must be expressed in *local coordinates*. This requires the use of the translation and rotation theorems (Section 2.3).

Given two scatterers  $\sigma_{n_0}$  and  $\sigma_{n_1}$  with their respective local coordinates systems centered at  $\mathbf{x}_{n_0}$  and  $\mathbf{x}_{n_1}$  (we assume they all have the same orientation for simplicity), we let  $A_{n_0}^{n_1}$  be the operator introduced in Theorems 2 and 3 that transforms the irregular sequence  $\{a_{l,m}^{n_1}\}$  representing the field scattered by  $\sigma_{n_1}$  into a regular sequence in which associated expansion is valid in  $\mathcal{B}_{|\mathbf{x}_{n_0}-\mathbf{x}_{n_1}|}(\mathbf{x}_{n_0})$  representing the same field in  $\sigma_{n_0}$ ’s local coordinates. We let  $A_{n_0}^0$  represent the same object for the case of the incident field  $u_0$ . Generally,  $u^0$  represents the field generated by point sources. In this case, we let  $a^0$  be its associated irregular sequence. In the case where  $u^0$  has no singularity (e.g. plane wave) we still use the notation  $a^0$  to denote its associated regular sequence. In any case, we obtain

$$b^{n_0} = A_{n_0}^0 a^0 + \sum_{\substack{n=1 \\ n \neq n_0}}^N A_{n_0}^n a^n$$

and,

$$u_{n_0}^i(\mathbf{x}) = \sum_{l=0}^{\infty} \sum_{m=-l}^l b_{l,m}^{n_0} j_l(k r_0(\mathbf{x})) Y_l^m(\hat{r}_0(\mathbf{x}))$$

where  $\mathbf{r}_0(\mathbf{x}) = \mathbf{x} - \mathbf{x}_{n_0}$ , which is now expressed in  $\sigma_{n_0}$ ’s local coordinates.  $\sigma_{n_0}$ ’s T-matrix can now be applied to provide the scattered field,

$$a^{n_0} = T^{n_0} A_{n_0}^0 a^0 + T^{n_0} \left( \sum_{\substack{n=1 \\ n \neq n_0}}^N A_{n_0}^n a^n \right)$$

$$= T^{n_0} A_{n_0}^0 a^0 + T^{n_0} [A_{n_0}^1, \dots, A_{n_0}^{n_0-1}, 0, A_{n_0}^{n_0+1}, \dots, A_{n_0}^N]$$

$$\begin{bmatrix} a^1 \\ \dots \\ a^{n_0-1} \\ a^{n_0} \\ a^{n_0+1} \\ \dots \\ a^N \end{bmatrix}.$$

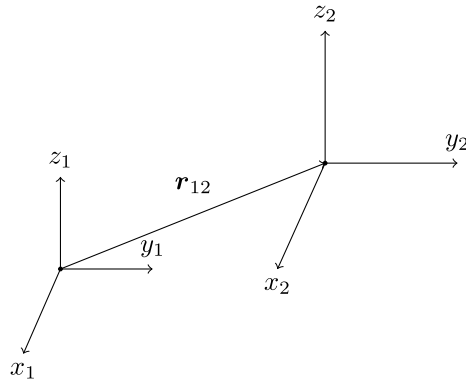


**Fig. 2.** Schematic of translation. An expansion in spherical wave function is translated along the vector linking the origin of two different coordinate systems having the same orientation.

Such a system of equations is obtained for each of the scatterer \$\sigma\_n, n = 1 \dots N\$. Putting everything in matrix form leads to,

$$\begin{bmatrix} a^1 \\ a^2 \\ \dots \\ a^N \end{bmatrix} = \begin{bmatrix} T^1 & & & \\ & T^2 & & \\ & & \dots & \\ & & & T^N \end{bmatrix} \left( \begin{bmatrix} A_1^0 \\ A_2^0 \\ \dots \\ A_N^0 \end{bmatrix} a^0 + \begin{bmatrix} 0 & A_1^2 & \dots & A_1^N \\ A_2^1 & 0 & \dots & A_2^N \\ \dots & \dots & \dots & \dots \\ A_N^1 & A_N^2 & \dots & 0 \end{bmatrix} \begin{bmatrix} a^1 \\ a^2 \\ \dots \\ a^N \end{bmatrix} \right)$$

which can be rewritten as,

$$(I - TA) a = TA^0 a^0$$

where \$I\$ represents the identity. The operator \$(I - TA)\$ is what is referred to as the Foldy–Lax system. Inverting it provides one with the vector of irregular sequences \$a\$ which characterizes the solution. We shall also refer to \$A\$ as the transfer operator.

### 2.3. Addition theorem, translation and rotation operators

We now introduce the explicit forms of the translation operators \$A\_i^j\$ discussed in the previous section. We also introduce rotation operators which will constitute the crux of an optimization step presented in Section 2.3.2.

#### 2.3.1. Translation operators

Broadly speaking, translation operators are a family of operators that take a SWF expansion associated with a particular coordinate system e.g. \$(x\_1, y\_1, z\_1)\$ in Fig. 2, and transforms it into another SWF expansion that corresponds to a different coordinate system with the same orientation (a translate of the former) e.g. \$(x\_2, y\_2, z\_2)\$ in Fig. 2.

Here, we are concerned with the nature of such operators together with their explicit representations. We are interested in two such representations: the dense representation, and the diagonal, or integral, representation.

To understand why two such representations are needed, we introduce the concepts of high-frequency (HF) regime and low-frequency (LF) regime. By high-frequency regime, we imply that the distance between the origins of the two coordinate systems between which a translation to be performed is larger than a wavelength in the background medium, i.e. \$|\mathbf{r}\_{12}| \gtrsim \lambda\_0\$. As for the low-frequency regime, it refers to translations between coordinate system in which distance is smaller or equal to a wavelength in the background, i.e. \$|\mathbf{r}\_{12}| \lesssim \lambda\_0\$. As we shall see, translations in the HF regime can be done in a very fast manner but suffer from numerical instability when the distance becomes too small. The use of a more robust but slower representation of translation operators is thus needed in the LF regime and appears as a trade-off between speed and accuracy. The starting point is the following theorem which is usually referred to as the *addition theorem* (Thm 3.26, Thm 3.27, [37]),

**Theorem 2.** Let \$\mathbf{r}\_1 = \mathbf{r}\_{12} + \mathbf{r}\_2\$. Then,

$$j_l(kr_1)Y_l^m(\hat{\mathbf{r}}_1) = \sum_{l'=0}^{\infty} \sum_{m'=-l'}^{l'} \beta_{(l',m')}^{(l,m)}(\mathbf{r}_{12}) j_{l'}(kr_2)Y_{l'}^{m'}(\hat{\mathbf{r}}_2), \quad \mathbf{r}_2 \in \mathbb{R}^3 \tag{7}$$

$$h_l^{(1)}(kr_1)Y_l^m(\hat{\mathbf{r}}_1) = \sum_{l'=0}^{\infty} \sum_{m'=-l'}^{l'} \beta_{(l',m')}^{(l,m)}(\mathbf{r}_{12}) h_{l'}^{(1)}(kr_2)Y_{l'}^{m'}(\hat{\mathbf{r}}_2), \quad |\mathbf{r}_2| > |\mathbf{r}_{12}| \tag{8}$$

$$h_l^{(1)}(kr_1)Y_l^m(\hat{\mathbf{r}}_1) = \sum_{l'=0}^{\infty} \sum_{m'=-l'}^{l'} \alpha_{(l',m')}^{(l,m)}(\mathbf{r}_{12}) j_{l'}(kr_2)Y_{l'}^{m'}(\hat{\mathbf{r}}_2), \quad |\mathbf{r}_2| < |\mathbf{r}_{12}| \tag{9}$$

where,

$$\beta_{(l',m')}^{(l,m)}(\mathbf{r}) = \sum_{l''=0}^{\infty} \sum_{m=-l''}^{l''} j_{l''}(kr) Y_{l''}^{m''}(\hat{\mathbf{r}}) \int_{\Omega} Y_l^m(\theta, \phi) \overline{Y_{l'}^{m'}}(\theta, \phi) \overline{Y_{l''}^{m''}}(\theta, \phi) 4\pi i^{l'+l''-l} d\Omega \tag{10}$$

$$\alpha_{(l',m')}^{(l,m)}(\mathbf{r}) = \sum_{l''=0}^{\infty} \sum_{m=-l''}^{l''} h_{l''}^{(1)}(kr) Y_{l''}^{m''}(\hat{\mathbf{r}}) \int_{\Omega} Y_l^m(\theta, \phi) \overline{Y_{l'}^{m'}}(\theta, \phi) \overline{Y_{l''}^{m''}}(\theta, \phi) 4\pi i^{l'+l''-l} d\Omega. \tag{11}$$

Upon writing,

$$\sum_{l=0}^{\infty} \sum_{m=-l}^l b_{l,m} j_l(kr_1) Y_l^m(\hat{\mathbf{r}}_1) = \sum_{l'=0}^{\infty} \sum_{m'=-l'}^{l'} \left[ \sum_{l=0}^{\infty} \sum_{m=-l}^l \beta_{(l',m')}^{(l,m)}(\mathbf{r}_{12}) b_{l,m} \right] j_{l'}(kr_2) Y_{l'}^{m'}(\hat{\mathbf{r}}_2)$$

it appears that such operators can be represented as infinite matrices acting on regular/irregular sequences. Eqs. (10), (11) show that the entries of such matrices will, for the most part, be nonzero resulting in fully populated matrices. Such matrices shall be truncated for computational purpose (see Section 2.3.2). Even so, it quickly becomes too expensive to apply such dense operators, and we shall only do so in the LF regime when it is not possible to use the faster diagonal form which we now introduce [56–58],

**Theorem 3.** Let  $\mathbf{r}_1 = (\mathbf{R}_{12} + \rho_{12}) + \mathbf{r}_2$ . Then,

$$j_l(kr_1) Y_l^m(\hat{\mathbf{r}}_1) = \sum_{l'=0}^{\infty} \sum_{m'=-l'}^{l'} \beta_{(l',m')}^{(l,m)}(\mathbf{r}_{12}) j_{l'}(kr_2) Y_{l'}^{m'}(\hat{\mathbf{r}}_2), \quad \mathbf{r}_2 \in \mathbb{R}^3 \tag{12}$$

$$h_l^{(1)}(kr_1) Y_l^m(\hat{\mathbf{r}}_1) = \sum_{l'=0}^{\infty} \sum_{m'=-l'}^{l'} \beta_{(l',m')}^{(l,m)}(\mathbf{r}_{12}) h_{l'}^{(1)}(kr_2) Y_{l'}^{m'}(\hat{\mathbf{r}}_2), \quad |\mathbf{r}_2| > |\mathbf{R}_{12} + \rho_{12}| \tag{13}$$

$$h_l^{(1)}(kr_1) Y_l^m(\hat{\mathbf{r}}_1) = \sum_{l'=0}^{\infty} \sum_{m'=-l'}^{l'} \alpha_{(l',m')}^{(l,m)}(\mathbf{r}_{12}) j_{l'}(kr_2) Y_{l'}^{m'}(\hat{\mathbf{r}}_2), \quad |\mathbf{r}_2| < |\mathbf{R}_{12} + \rho_{12}| \tag{14}$$

where,

$$\beta_{(l',m')}^{(l,m)}(\mathbf{r}) = \int_{\Omega} i^{l'-l} Y_l^m(\hat{\mathbf{s}}) \overline{Y_{l'}^{m'}}(\hat{\mathbf{s}}) e^{i k(\mathbf{R}_{12} + \rho_{12}) \cdot \hat{\mathbf{s}}} d\Omega(\hat{\mathbf{s}}) \tag{15}$$

$$\alpha_{(l',m')}^{(l,m)}(\mathbf{r}) = \lim_{N \rightarrow \infty} \int_{\Omega} i^{l'-l} Y_l^m(\hat{\mathbf{s}}) \left( \sum_{n=0}^N i^n (2n+1) h_n^{(1)}(kR_{12}) P_n(\hat{\mathbf{R}}_{12} \cdot \hat{\mathbf{s}}) \right) \overline{Y_{l'}^{m'}}(\hat{\mathbf{s}}) e^{i k \rho_{12} \cdot \hat{\mathbf{s}}} d\Omega(\hat{\mathbf{s}}). \tag{16}$$

**Remark.** The splitting of the vector  $\mathbf{r}_{12}$  into the sum  $\mathbf{R}_{12} + \rho_{12}$  in Theorem 3 is related to the spatial decomposition used by the FMM (octree; Section 2.4) and is not unique. It has been introduced here in preparation for the algorithmic considerations presented in Section 2.4.

To grasp the full potential of this representation, let  $\mathbf{r}_1 = \mathbf{r}_{12} + \mathbf{r}_2 = (\mathbf{R}_{12} + \rho_{12}) + \mathbf{r}_2$ . Using Eqs. (14), (16) one finds that the coefficients of the irregular sequence associated with the expansion about the new coordinate system take the form,

$$b_{l,m} = \lim_{N \rightarrow \infty} \int_{\Omega} \left( \sum_{l=0}^{\infty} \sum_{m=-l}^l \frac{1}{l!} a_{l,m} Y_l^m(\hat{\mathbf{s}}) \right) e^{i k \rho_{12} \cdot \hat{\mathbf{s}}} \left( \sum_{n=0}^N i^n (2n+1) h_n^{(1)}(kR_{12}) P_n(\hat{\mathbf{R}}_{12} \cdot \hat{\mathbf{s}}) \right) i^{l'} \overline{Y_{l'}^{m'}}(\hat{\mathbf{s}}) d\Omega(\hat{\mathbf{s}})$$

from which we recognize three operations,

- (i) A spherical harmonics transform of the irregular sequence:  $\sum_{l=0}^{\infty} \sum_{m=-l}^l a_{l,m} i^{-l} Y_l^m(\hat{\mathbf{s}})$ .
- (ii) A HF translation:  $e^{i k \rho_{12} \cdot \hat{\mathbf{s}}} \sum_{n=0}^{N_0} i^n (2n+1) h_n^{(1)}(kR_{12}) P_n(\hat{\mathbf{R}}_{12} \cdot \hat{\mathbf{s}})$ .
- (iii) An inverse spherical harmonics transform:  $b_{l,m} = \int_{\Omega} (\cdot) i^{l'} \overline{Y_{l'}^{m'}}(\hat{\mathbf{s}}) d\Omega(\hat{\mathbf{s}})$ .

The most important point is that the HF translation appears as a mere *multiplication* by a function on the sphere and is therefore a *diagonal* operator. This is very attractive from a computational viewpoint. Indeed, it is shown in Section 2.3.7 that spherical harmonics transforms (SHT) can be carried out in low computational (linear) complexity. Together, this fact and the diagonal nature of the translation operator implies that the whole translation can be applied in low complexity (Section 2.3.6).

### 2.3.2. Translation operators; finite representation

We now discuss the practical representations of wave fields in the low- and high-frequency regimes; the results of the previous sections provide us with such representations in the form of an infinite sequence and a function defined on the unit sphere  $\mathcal{B}_1(\mathbf{0})$  in each case respectively. However, from a computational standpoint neither can be handled; the infinite sequence must be truncated and the function on the unit sphere must be represented through a finite set of points. When and how to truncate is a subject of research in itself. For the problem at hand, an in-depth analysis can be found in [47]. See also [59]. We decided to omit the details in the current document in order to concentrate on the theme of our algorithm.

### 2.3.3. Low-frequency regime

In the low frequency regime, *truncated* regular and irregular sequences  $\{a_{l,m}\}_{\substack{l=0 \\ |m|\leq l}}^L$  and  $\{b_{l,m}\}_{\substack{l=0 \\ |m|\leq l}}^L$  are used to represent the field through SWF expansion,

$$\sum_{l=0}^L \sum_{m=-l}^l a_{l,m} j_l(k_0 r) Y_l^m(\hat{\mathbf{r}}) + \sum_{l=0}^L \sum_{m=-l}^l b_{l,m} h_l^{(1)}(k_0 r) Y_l^m(\hat{\mathbf{r}}).$$

In this representation the translation operator takes the form of a dense matrix. In this sense, the truncation of the tails of each sequence implies that this infinite matrix of [Theorem 2](#) is replaced by a finite one, namely, its principal minor (upper-left corner). This matrix remains dense however and being such, it is expensive to apply. For this reason, we introduce in [Section 2.3.6](#) ways of reducing the computational cost of applying it.

### 2.3.4. High-frequency regime

The HF portion of the code constitutes a generalization of the method presented by Cecka & Darve [42]. For this reason, it is recommended that the reader be familiar with the latter. In this section, we shall elaborate on the modifications required for the method to be used in our context. First, recall that in the HF regime the translation coefficients take the form,

$$\beta_{(l',m')}^{(l,m)}(\mathbf{r}) = \int_{\Omega} i^{l'-l} Y_l^m(\hat{\mathbf{s}}) \overline{Y_{l'}^{m'}(\hat{\mathbf{s}})} e^{i k(\mathbf{R}_{12} + \rho_{12}) \cdot \hat{\mathbf{s}}} d\Omega(\hat{\mathbf{s}})$$

$$\alpha_{(l',m')}^{(l,m)}(\mathbf{r}) = \lim_{N \rightarrow \infty} \int_{\Omega} i^{l'-l} Y_l^m(\hat{\mathbf{s}}) \left( \sum_{n=0}^N i^n (2n+1) h_n^{(1)}(kR_{12}) P_n(\hat{\mathbf{R}}_{12} \cdot \hat{\mathbf{s}}) \right) \overline{Y_{l'}^{m'}(\hat{\mathbf{s}})} e^{i k \rho_{12} \cdot \hat{\mathbf{s}}} d\Omega(\hat{\mathbf{s}}).$$

From a computational perspective, the crux of this representation lies in a proper truncation of the infinite series, and an adequate discretization of the integral. Such discretization leads to expression of the form,

$$\beta_{(l',m')}^{(l,m)}(\mathbf{r}) = \sum_p w_p i^{l'-l} Y_l^m(\hat{\mathbf{s}}_p) \overline{Y_{l'}^{m'}(\hat{\mathbf{s}}_p)} e^{i k(\mathbf{R}_{12} + \rho_{12}) \cdot \hat{\mathbf{s}}_p} \tag{17}$$

$$\alpha_{(l',m')}^{(l,m)}(\mathbf{r}) = \lim_{N \rightarrow \infty} \sum_p w_p i^{l'-l} Y_l^m(\hat{\mathbf{s}}_p) \left( \sum_{n=0}^N i^n (2n+1) h_n^{(1)}(kR_{12}) P_n(\hat{\mathbf{R}}_{12} \cdot \hat{\mathbf{s}}_p) \right) \overline{Y_{l'}^{m'}(\hat{\mathbf{s}}_p)} e^{i k \rho_{12} \cdot \hat{\mathbf{s}}_p} \tag{18}$$

which involves finitely many points. Now recall from [Section 2.3.1](#) that application of the translation operator in the HF regime requires a forward and backward spherical harmonics transform ([Section 2.3.7](#)),

$$\phi(\hat{\mathbf{s}}) = \sum_{l=0}^{\infty} \sum_{m=-l}^l a_{l,m} i^{-l} Y_l^m(\hat{\mathbf{s}})$$

which following the discretization, must only be known at the points,

$$\{\phi(\hat{\mathbf{s}}_p)\}_p.$$

This finite set of points is what we refer to as the *high-frequency representation*. It is called regular if it originates from a regular sequence and irregular if it originates from an irregular sequence.

Finding an adequate  $N$  in [Eq. \(18\)](#) that will result in a small error and numerical stability has been the subject of extensive research which can be found in [60,57,59]. It is also discussed at length in [42], so we shall not repeat the discussion here. We just briefly mention that the choice of  $N$  has relatively little effect on the computational cost but rather constitutes a trade-off between numerical error and numerical stability.

Once a proper value for  $N$  has been chosen, one must devise an appropriate way of discretizing the remaining integral. In this sense, the main idea of Cecka & Darve [42] is to proceed to a “doubling of the sphere”, that is, extending the domain

of  $\theta$  from  $[0, \pi]$  to  $[0, 2\pi]$ . In their notation,  $\mathbf{r} = \mathbf{R}_{12} + \rho_{12}$  and  $\alpha_{(\ell', m')}^{(l, m)}(\mathbf{r})$  takes the form,

$$\alpha_{(\ell', m')}^{(l, m)}(\mathbf{r}) = \frac{4\pi}{ik} \int_0^{2\pi} \int_0^{2\pi} i^{-l} Y_l^m(\theta, \phi) E_{\mathbf{r}_{12}}(\theta, \phi) T_{N, \mathbf{R}_{12}}(\theta, \phi) \frac{1}{2} |\sin(\theta)| i^{\ell'} \overline{Y_{\ell'}^{m'}}(\theta, \phi) \, d\theta \, d\phi$$

where,

$$E_{\mathbf{r}_{12}}(\theta, \phi) = e^{ikr_{12} \cdot \hat{\mathbf{s}}(\theta, \phi)}$$

$$T_{N, \mathbf{R}_{12}}(\theta, \phi) = \frac{ik}{4\pi} \sum_{n=0}^N i^n (2n + 1) h_n^{(1)}(kR_{12}) P_n(\hat{\mathbf{s}} \cdot \hat{\mathbf{R}}_{12}).$$

The authors then describe how it is possible, by filtering of the integrand and through the use of a trapezoid rule, to obtain an effective quadrature. Following their description, we write,

$$T_{N, \mathbf{R}_{12}}^s(\theta, \phi) = \frac{1}{2} T_{N, \mathbf{R}_{12}}(\theta, \phi) |\sin(\theta)|$$

$$T_{N, \mathbf{R}_{12}}^{s, N_\theta}(\theta, \phi) = \sum_{|n| \leq \frac{N_\theta}{2} - 1} \mathcal{F}_n^\theta [T_{N, \mathbf{R}_{12}}^s](\phi) e^{in\theta}.$$

The quantity to be computed numerically as an approximation to  $\alpha_{(\ell', m')}^{(l, m)}(\mathbf{r})$  above takes the form,

$$\tilde{\alpha}_{(\ell', m')}^{(l, m)}(\mathbf{r}) = \frac{4\pi}{ik} \frac{4\pi^2}{N_\theta N_\phi} \sum_{n=1}^{N_\theta} \sum_{m=1}^{N_\phi} i^{-l} Y_l^m(\theta_n, \phi_m) E_{\mathbf{r}_{12}}(\theta_n, \phi_m) T_{N, \mathbf{R}_{12}}^{s, N_\theta}(\theta_n, \phi_m) i^{\ell'} \overline{Y_{\ell'}^{m'}}(\theta_n, \phi_m) \tag{19}$$

where,

$$\theta_n = \frac{2\pi n}{N_\theta}, \quad \phi_m = \frac{2\pi m}{N_\phi}$$

$N_\theta$  and  $N_\phi$  being integers whose determination is described in detail in [42] and [47, Section 7.1.2]. This is the expression obtained by approximating the original integral through a trapezoid rule in both  $\theta$  and  $\phi$  after substituting  $T_{N, \mathbf{R}_{12}}^s(\theta, \phi)$  in the integrand by a bandlimited version  $T_{N, \mathbf{R}_{12}}^{s, N_\theta}(\theta, \phi)$ .

### 2.3.5. Rotation operators

In a manner similar to that of the translation operators (see Fig. 3), rotation operators take a SWF expansion associated with a particular coordinate system and transform it into another SWF expansion that corresponds to a rotated coordinate system with the same origin. The existence of such operator has been proved in [61]. An explicit representation is the subject of the next theorem, (Appendix C [37], see also [62–64]).

**Theorem 4.** *Let  $(r_1, \theta_1, \phi_1)$  and  $(r_2, \theta_2, \phi_2)$  be two spherical coordinate systems sharing the same origin and  $(\alpha, \beta, \gamma)$  be the Euler angles relating both systems. Then,*

$$Y_l^m(\theta_1, \phi_1) = \sum_{m'=-l}^l D_{(\ell', m')}^{(l, m)}(\alpha, \beta, \gamma) Y_{\ell'}^{m'}(\theta_2, \phi_2) \tag{20}$$

where,

$$D_{(\ell', m')}^{(l, m)}(\alpha, \beta, \gamma) = e^{-l\alpha} d_{(\ell', m')}^{(l, m)}(\beta) e^{-im\gamma} \tag{21}$$

$d_{(\ell', m')}^{(l, m)}(\beta)$  is such that,

$$d_{(\ell', m')}^{(l, m)}(\beta) = (-1)^{m+l} \overline{d_{(\ell', m')}^{(-l, -m)}(\beta)}$$

and equal to,

$$d_{(\ell', m')}^{(l, m)}(\beta) = \sum_{k=0}^{l-m'} (-1)^{k+m+m'} \frac{\sqrt{(l+m')!(l-m')!(l+m)!(l-m)!}}{(l-m'-k)!(l+m-k)!(k+m'-m)!k!} (\cos(\beta))^{2l} \left( \tan\left(\frac{\beta}{2}\right) \right)^{2k+m'-m} \tag{22}$$

for  $m + m' \geq 0$ .

It is interesting to note that the sum in Eq. (20) only involves orders  $|m| \leq l$ . When put in matrix form, this results in a block diagonal matrix which can be applied in a fast manner (Section 2.3.2).

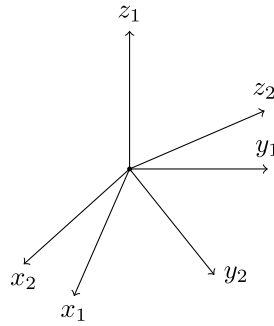


Fig. 3. Schematic of rotation. An expansion in spherical wave function is rotated about the fixed origin of two different coordinate systems.

2.3.6. Low-frequency optimization; the point-and-shoot method

The starting point of the optimization lies in the following lemma whose proof can be found in [62],

**Lemma 1.** For any  $0 < r \in \mathbb{R}$  we have,

$$\beta_{(l',m')}^{(l,m)}(r\hat{\mathbf{z}}) = \alpha_{(l',m')}^{(l,m)}(r\hat{\mathbf{z}}) = 0$$

whenever  $m' \neq m$ , and where  $\beta_{(l',m')}^{(l,m)}, \alpha_{(l',m')}^{(l,m)}$  as defined in Theorem 2.

This means that the matrix corresponding to a translation along the z-axis is sparse. This fact can be exploited in order to speed up computations. This can be done as follows: every translation in the LF regime is first transformed into a translation along the z-axis in a rotated coordinate system through the use of the rotation operators (see Section 2.3 and below). Then, the translation is done at low cost thanks to Lemma 1 and the inverse rotation is applied to recover the expansion in the original coordinate system.

We shall use the notation of Edmonds [62] to denote rotations by which,

$$D(\gamma, \beta, \alpha)$$

represents a passive rotation of a coordinate system in  $\mathbb{R}^3$  by  $\alpha$  about the original z-axis, followed by a rotation by  $\beta$  about the resulting y-axis, followed by a rotation by  $\gamma$  about the resulting z-axis. By passive, we mean that the coordinate system is rotated but the objects of interest i.e. functions defined on  $\mathbb{R}^3$ , remain unchanged. In other words, points are simply reassigned new coordinates.

Such rotations further induce rotations in function space (see [62] for details). That is, if  $\mathbf{r} = (r_1, r_2, r_3)$  corresponds to a vector in  $\mathbb{R}^3$  and  $D\mathbf{r} = \mathbf{r}' = (r'_1, r'_2, r'_3)$  represents this same vector in a new coordinate system associated with the rotation  $D = D(\gamma, \beta, \alpha)$ , then for each function  $f(\mathbf{x})$  defined on  $\mathbb{R}^3$  there exists a unique function  $f'(\mathbf{x}')$  such that,

$$f'(\mathbf{x}') = f'(D\mathbf{x}') = f(\mathbf{x}), \quad \forall \mathbf{x} \in \mathbb{R}^3.$$

The map,  $\mathcal{D}f = f'$  thus appears as the rotation in function space.

When  $f(\cdot)$  is a linear combination of spherical wave functions, the operator  $\mathcal{D}$  has a known explicit form and corresponds to the rotation matrices introduced in Section 2.3.5. However, unless the rotation matrices can be applied at low cost the advantage of a sparse translation matrix along the z-axis will be lost. Fortunately, this can be achieved through the following decompositions (see [62]),

$$\begin{aligned} \mathcal{D}(\gamma, \beta, \alpha) &= \mathcal{D}(\gamma, 0, 0) \mathcal{D}(0, \beta, 0) \mathcal{D}(0, 0, \alpha) \\ \mathcal{D}(0, \beta, 0) &= \mathcal{D}\left(-\frac{\pi}{2}, 0, 0\right) \mathcal{D}\left(0, -\frac{\pi}{2}, 0\right) \mathcal{D}(\beta, 0, 0) \mathcal{D}\left(0, \frac{\pi}{2}, 0\right) \mathcal{D}\left(\frac{\pi}{2}, 0, 0\right) \end{aligned}$$

and the explicit representations (Note that since rotations do not affect the radial component, it is sufficient to consider the operators acting on spherical harmonics only.),

$$\begin{aligned} \int_{\Omega} (\mathcal{D}(0, 0, \alpha) Y_l^m(\theta, \phi)) \bar{Y}_{l'}^{m'}(\theta, \phi) d\Omega &= \begin{cases} e^{im\alpha} & \text{if } m = m' \\ 0 & \text{if } m \neq m' \end{cases} \\ \int_{\Omega} (\mathcal{D}(\gamma, 0, 0) Y_l^m(\theta, \phi)) \bar{Y}_{l'}^{m'}(\theta, \phi) d\Omega &= \begin{cases} e^{im\gamma} & \text{if } m = m' \\ 0 & \text{if } m \neq m' \end{cases} \\ \int_{\Omega} (\mathcal{D}(0, \pm\frac{\pi}{2}, 0) Y_l^m(\theta, \phi)) \bar{Y}_{l'}^{m'}(\theta, \phi) d\Omega &= \begin{cases} [\delta]_{(l,m')}^{(l,m)}(\pm\pi/2) & \text{if } l = l' \\ 0 & \text{if } l \neq l' \end{cases} \end{aligned}$$

where,

$$[\delta]_{(l,m')}^{(l,m)}(\pm\pi/2) = \sqrt{\frac{(l+m')!(l-m')!}{(l+m)!(l-m)!}} \sum_k \binom{l+m}{l-m'-k} \binom{l-m}{k} (-1)^{l-m'-k} \cdot (\cos(\pm\pi/4))^{2k+m'+m} (\sin(\pm\pi/4))^{2l-2k-m'-m}.$$

This shows that every rotation matrix can be decomposed into the product of 7 matrices, 5 of which are *diagonal*. The remaining two matrices ( $\mathcal{D}(0, \pm\frac{\pi}{2}, 0)$ ) are *sparse* since their entries are 0 unless  $l = l'$ . These identities are just special cases of the general formulas introduced in Section 2.3.5. Letting,

$$\mathcal{R} = D\left(-\frac{\pi}{2}, 0, 0\right) D\left(0, -\frac{\pi}{2}, 0\right) D(\theta, 0, 0) D\left(0, \frac{\pi}{2}, 0\right) D\left(\frac{\pi}{2}, 0, 0\right) D(0, 0, \phi)$$

and putting everything together, it follows that any translation matrix can be written as,

$$\mathcal{R}^\dagger \cdot T_z(r) \cdot \mathcal{R}$$

where  $T_z(r)$  represents a translation along the  $z$ -axis at distance  $r$ , and  $\dagger$  represents the Hermitian transpose.

Finally, there remains the question of computing the entries of these matrices. Those of the form  $\mathcal{D}(\gamma, 0, 0)$ ,  $\mathcal{D}(0, 0, \alpha)$  pose no problem. As for  $D(0, \pm\frac{\pi}{2}, 0)$  and  $T_z(r)$  one could use the formulas introduced in Eqs. (22) and (11) respectively. Unfortunately, the use of these formulas can be slow and unstable at times. For this reason, we preferred to use recurrence relations in order to compute the coefficients. The scheme we used is presented in great detail in [64].

### 2.3.7. Interface

Conversion between LF representation (finite regular/irregular sequence; Section 2.3.3) and the HF representation (FMM far field expansion; Section 2.3.4) of a field can be performed rapidly using the FFT. Algorithms are presented in Algorithm 1–2. We omit the details here and refer the reader to [47] for a more thorough description of these simple procedures.

```

1 for n from 1 to Nθ do
2   for m from -L to L do
3     Compute  $\chi_m^n = \sum_{l=|m|}^L \frac{a_{l,m}}{l^{l+1}} \sqrt{\frac{2l+1}{4\pi}} \frac{(l-m)!}{(l+m)!} P_l^m(\cos(\theta_n))$ 
4 for n from 1 to Nθ do
5   Compute  $\psi_a(\theta_n, \phi_m) = \sum_{\mu=-L}^L \chi_\mu^n e^{i\mu\phi_m}$  for  $m = 1, \dots, N_\phi$  through IFFT

```

**Algorithm 1:** Forward Spherical Harmonics Transform algorithm from a finite sequence  $\{a_{l,m}\}$  to a FMM far field expansion  $\{\psi_a(\theta_n, \phi_m)\}$

```

1 for n from 1 to Nθ do
2   Compute  $\chi_m^n = \sum_{\mu=1}^{N_\phi} \frac{4\pi}{N_\theta N_\phi} \psi(\theta_n, \phi_\mu) e^{-m\phi_\mu}$  for  $m = -L, \dots, L$  through FFT.
3 for l from 0 to L do
4   for m from -l to l do
5     Compute  $b_{l,m} = l^{l+1} \sum_{n=1}^{N_\theta} \chi_m^n \sqrt{\frac{2l+1}{4\pi}} \frac{(l-m)!}{(l+m)!} P_l^m(\cos(\theta_n)) \sin(\theta_n)$ 

```

**Algorithm 2:** Backward Spherical Harmonics Transform algorithm from FMM far field expansion  $\psi_b$  to finite sequence  $\{b_{l,m}\}$

## 2.4. Structure of the code and implementation

In this section, we provide details pertaining to the algorithmic structure of the code. First, we introduce the octree, a tree data structure underlying the whole method. Then, we describe how the operators discussed in Section 2.3 can be used, together with the tree structure, to apply the dense operator  $A$  in a fast manner.

Note that FMM tree-based codes share many characteristics as per their structure, the main difference generally lying with the nature of the translation/rotation operators involved. For this reason, most of what is presented in Section 2.4.1 can also be found in other work. We refer to [65,66] for some alternative presentations.

The wideband nature of the code implies that it is capable of handling problems which lie in both the high-frequency (HF) regime and the low-frequency (LF) regime (see Section 2.1). We recall that the HF regime corresponds broadly to a problem where the distance between any two scatterers lies above one wavelength in the background medium  $\lambda_0$  whereas the remainder falls into the LF regime (see Section 2.4.1 for a precise definition). To achieve this goal, our algorithm uses different representations of the fields and translation operators depending on the regime.

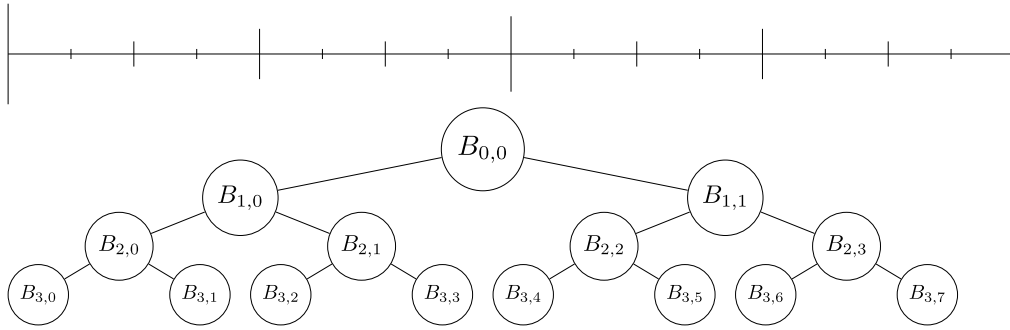


**Fig. 4.** Binary tree structure.  $B_{p,q} = [q2^{-l}, (q + 1)2^{-l}]$  represents the  $q$ th subinterval at level  $p$ .

In the HF regime, we use the form presented in Theorem 3 of Section 2.3 which constitutes an *integral representation* of the translation operator. Care must be taken in order to obtain a *discrete* representation fit for computational purposes as described in Section 2.3.4. This involves truncating the infinite series and discretizing the integral, and can be done in various manners e.g. [65]. In the present paper we decided to use the method presented by Cecka & Darve [42]. This method presents advantages over other choices which are detailed in Section 2.3.4. As with all current discretization techniques however, one important drawback is that the method has been developed for point scatterers only ( $l = m = 0$ ) and needs some adaptations in order to be used with finite size scatterers.

Translation operators in integral form unfortunately suffer from numerical instability when the translation distance falls roughly below a wavelength in the background. This is originally where a necessary distinction between HF and LF regime arises. For this reason, a different representation must be used in the LF regime. This is provided by Theorem 2 of Section 2.3. In this case, the operators take the form of *dense infinite matrices* which must be truncated (Section 2.3.3). The application of translation operators in this form is numerically stable yet slower than for the diagonal form due to their dense nature, although there remain ways of reducing the computational cost (Section 2.3.6).

Finally, an interface is needed to go between the HF and LF regimes. This is provided by a spherical harmonics transform. Again, optimizations exist to make this step faster and are presented in Section 2.3.7.

### 2.4.1. Tree-based algorithm

We first introduce the tree structure underlying the algorithm. We shall assume without loss of generality that all scatterers belong to a square domain  $\mathcal{S}$  of side 1. Such decomposition is generally referred to as an *octree* and constitutes a tree graph. The number of recursion depends on the number of scatterers present in  $\mathcal{S}$ . Generally,  $O(\log N)$  levels are used so that each of the smallest boxes contains  $O(1)$  scatterers.

We then need to make a few definitions. For clarity, we will use a binary tree structure (1D version of octree) to introduce our definitions although they carry to 2D and 3D in an obvious manner. The subdivisions and tree structure are shown in Fig. 4 at the top and bottom respectively.

We can now introduce the necessary definitions:

- (i) Given a box  $B_{p,q}$  at level  $p \neq 0$ , we define its *parent* set  $\mathcal{P}(B_{p,q})$  to be the box at level  $(p - 1)$  that contains it. For instance, in Fig. 4,  $\mathcal{P}(B_{3,3}) = \{B_{2,1}\}$ .
- (ii) Given a box  $B_{p,q}$  at level  $p \neq P$ , we define its *children* set  $\mathcal{C}(B_{p,q})$  to be the boxes at level  $(p + 1)$  that are contained within  $B_{p,q}$ . For instance, in Fig. 4,  $\mathcal{C}(B_{2,1}) = \{B_{3,2}, B_{3,3}\}$ .
- (iii) Given a box  $B_{p,q}$ , we define  $\mathcal{N}(B_{l,m})$  to be the *neighbor* set of boxes at level  $l$  which are adjacent to  $B_{l,m}$  together with  $B_{p,q}$  itself. For instance, in Fig. 4,  $\mathcal{N}(B_{3,3}) = \{B_{3,2}, B_{3,3}, B_{3,4}\}$ .
- (iv) Given a box  $B_{p,q}$ , we define  $\mathcal{I}(B_{p,q})$  to be the *interaction list* of boxes at level  $p$  which are not the neighbors of  $B_{p,q}$  but whose parent is a neighbor of  $B_{p,q}$ 's parent. For instance, in Fig. 4,  $\mathcal{I}(B_{3,3}) = \{B_{3,0}, B_{3,1}, B_{3,5}\}$ . Two boxes that are in each other's interaction list will be called *well-separated*.

We will say that a box belongs to the HF regime if its sidelength is larger than a wavelength in the background medium ( $\lambda_0$ ). Similarly, a box will lie in the LF regime if its sidelength is smaller than a wavelength in the background medium ( $\lambda_0$ ). A scatterer belongs to the HF regime if the leaf box to which it belongs lies in the HF regime and to the LF regime otherwise.

To each box  $B_{l,m}$  in the octree and each scatterer  $\sigma_n$  in the system we assign two types of field representations depending on the regime, they are:

- (i) Low-frequency representations (Section 2.3.3)
  - (a) A *regular Low-frequency representation* of the field *incident* onto  $B_{l,m}$ ; this corresponds to a regular sequence  $\{b_{l,m}\}$  associated with a RSWF series used to represent the field in a neighborhood of  $B_{l,m}$ .
  - (b) An *irregular Low-frequency representation* of the field *scattered* by the obstacles in  $B_{l,m}$ ; this corresponds to an irregular sequence  $\{a_{l,m}\}$  associated with an ISWF series used to represent the scattered field outside of  $B_{l,m}$ .

(ii) High-frequency representations (Section 2.3.4)

- (a) A *regular High-frequency representation* of the field incident onto  $B_{l,m}$ ; this corresponds to a sampling of the far-field signature  $\{\phi(\hat{s}_k)\}_k$  of the field representing the incident field onto  $B_{l,m}$  in a neighborhood of  $B_{l,m}$ .
- (b) An *irregular High-frequency representation* of the field scattered by the obstacles in  $B_{l,m}$ ; this corresponds to a sampling of the far-field signature  $\{\phi(\hat{s}_k)\}_k$  used to represent the scattered field outside of  $B_{l,m}$ .

All representations are associated with a coordinate system with origin at the center of the box (scatterer respectively). It is important to note that representations associated with an incident field are only valid in some *neighborhood* of the origin, whereas those associated with a scattered field are valid *away* from the origin. This is consistent with the range of validity of the translated expansions in [Theorems 2](#) and [3](#).

We finally introduce a last piece of terminology; we shall refer to the translation of an irregular field representation to an irregular field representation as a *multipole-to-multipole* (M2M) translation (LF: Eq. (8), HF: Eq. (13)). A translation of a regular field representation to a regular field representation will be called a *local-to-local* (L2L) translation (LF: Eq. (7), HF: Eq. (12)), and finally we will denote by *multipole-to-local* (M2L) the translation from an irregular to a regular field representation (LF: Eq. (9), HF: Eq. (14)). The exact nature of the operator to be used (dense or integral version) depends on the regime; the dense version described in Section 2.3.2 is used whenever one of the representation involved belongs to the low-frequency regime and the integral version of Section 2.3.4 is used otherwise.

At this point, we are now ready to give a complete description of the algorithm (see Algorithm 3) which consists in the following steps: Gather (1–3), Upward pass (4–6), Transfer (7–9), Downward pass (10–12), Scatter (13–15), Close-term interactions (16–17).

```

1 for each box at the leaf level  $\{B_{leaf,q}\}_{q=1}^{N_{leaf}}$  do
2   for each scatterer  $\sigma_n^{(p)}$  belonging to  $B_{leaf,q}$  do
3     Apply the M2M operator between the scatterer  $\sigma_n^{(q)}$  and the box to which it belongs  $B_{leaf,q}$ .
4 for each level  $p = leaf, \dots, 2$  do
5   for each box  $B_{p,q}$  at level  $p$  do
6     Apply the M2M operator between the box  $B_{p,q}$  and its parent box  $\mathcal{P}(B_{p,q})$ .
7 for each level  $l = leaf, \dots, 2$  do
8   for each box  $B_{p,q}$  at level  $p$  do
9     Apply the M2L operator between the box  $B_{p,q}$  and the members of its interaction list  $\mathcal{N}(B_{p,q})$ .
10 for each level  $l = 2, \dots, (leaf - 1)$  do
11   for each box  $B_{p,q}$  at level  $p$  do
12     Apply the L2L operator between the box  $B_{p,q}$  and its children boxes  $\mathcal{C}(B_{p,q})$ .
13 for each box at the leaf level  $\{B_{leaf,q}\}_{q=1}^{N_{leaf}}$  do
14   for each scatterer  $\sigma_n^{(q)}$  belonging to  $B_{leaf,q}$  do
15     Apply the L2L from the box to which it belongs  $B_{leaf,q}$  to the scatterer  $\sigma_n^{(q)}$ .
16 for each box at the leaf level  $\{B_{leaf,q}\}_{q=1}^{N_{leaf}}$  do
17   Directly compute the interactions between all the scatterers  $\sigma_n^{(q)}$  belonging to  $B_{leaf,q}$  and those belonging to its neighbor boxes  $\mathcal{N}(B_{leaf,q})$ .

```

**Algorithm 3:** Pseudo-code for the fast application of A. Gather (1–3), Upward pass (4–6), Transfer (7–9), Downward pass (10–12), Scatter (13–15), Close-term interactions (16–17).

## 2.5. Error analysis

Given  $N$  discrete scatterers with ISWF expansions  $\left\{ \{a_{l,m}^{(n)}\}_{n=1}^N \right\}$ , we measure the error in the norm,

$$\| \{a_{l,m}^{(n)}\}_n \|_{W_2^N(kR^{(n)})} = \sum_{n=1}^N \left( \sum_{l=0}^{\infty} \sum_{m=-l}^l |a_{l,m}^{(n)} h_l^{(1)}(kR^{(n)})|^2 \right)^{1/2} \quad (23)$$

where  $R^{(n)}$  is the smallest radius of a sphere sharing the same center as scatterer  $n$  and completely enclosing it. In particular, this norm leads to a *pointwise error estimate* between the computed scattered field and the exact solution in all of  $\mathbb{R}^3$  as shown in [47].

The correctness of our implementation has been verified through a series of tests [47] including comparison with an open-source BEM solver (Acousto, [67]). We have further carried out a complete error analysis of the algorithm based on the aforementioned norm [47]. Our choice of parameters is based on the estimates obtained following this analysis. However,

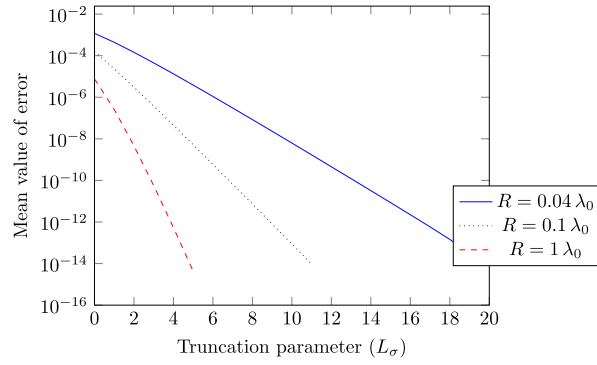


**Fig. 5.** Average value (angular) of the error (in the norm Eq. (23)) in the field produced by two scatterers (z-direction plane wave with wavelength  $\lambda_0$ ) with radius  $r = 0.01\lambda_0$ , speed of sound  $c = 0.2c_0$  and density  $\rho = 0.5\rho_0$  for which the centers are separated by a distance of  $R = \{0.04\lambda_0, 0.1\lambda_0, 1\lambda_0\}$ .

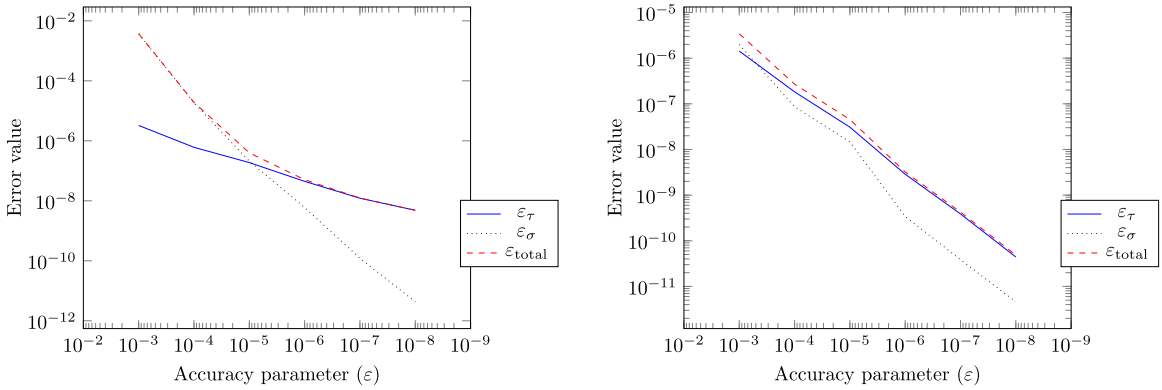


**Fig. 6.** Relative error incurred by algorithm following our choice of parameters described in [47]. Left: four-level tree, low-frequency regime. Number of scatterers:  $N = 35\,000$ , Scatterer speed of sound  $c = 0.1$ , Scatterer density  $\rho = 0.3$ , Scatterer radius  $r = 0.005$ , Cluster radius  $R = 0.5$ . Right: three-level tree, high-frequency regime. Number of scatterers:  $N = 5\,000$ , Scatterer speed of sound  $c = 6$ , Scatterer density  $\rho = 8$ , Scatterer radius  $r = 0.6$ , Cluster radius  $R = 25$ .  $\varepsilon_\sigma$  represents the error associated with the truncation parameter  $L_\sigma$ ,  $\varepsilon_\tau$  represents the error associated with the truncation parameter  $L_\tau$  and  $\varepsilon_{\text{total}}$  is the total error (sum).

since this paper is concerned with the algorithm, and due to the lengthy treatment and somewhat technical nature of the subject, we only discuss the topic briefly. We strongly recommend the interested readers to refer to [47].

For discretization purposes, our algorithm requires the choice of three different types of truncation parameters:

- The truncation parameter  $L_\sigma$  for the SWF expansion of *each* scatterers (sum truncation; Eq. (5)).
- The truncation parameter  $L_\tau$  for the SWF expansion at *each level of the tree* (sum truncation; Eqs. (7)–(16)).
- The quadrature in the *high-frequency regime* (integral discretization; Eq. (19)).

We have derived (somewhat conservative) error bounds for each quantity. These allow us to choose these various parameters according to the desired accuracy ( $\varepsilon$ ) in the norm found in Eq. (23). In short, all three types of error decay *exponentially fast* as we increase the number of degrees of freedom. Figs. 5 and 6 show examples. Fig. 5 shows the behavior (exponential decay) of the error between the computed field and a high-accuracy field resulting from a plane wave traveling in the z-direction averaged over various configurations of a two-sphere cluster, as a function of the truncation parameter  $L_\sigma$ . Fig. 6 shows the error behavior of the full algorithm in the low-frequency (left) and high-frequency (right) regimes as a function of the desired accuracy ( $\varepsilon$ ) and upon choosing all parameters following the scheme presented in [47] which is based on the error analysis. The results are in agreement with the expected behavior.

## 2.6. Scaling

In this section, we present results regarding the  $\mathcal{O}(N)$  scaling of our scheme. Such scaling is of utmost importance for this type of simulation. Indeed, each simulation presented in this section for instance contains roughly  $N = \mathcal{O}(10^6)$  unknowns. A linear scaling implies that approximately  $\mathcal{O}(10^7)$  flops are necessary to compute a single matrix–vector product within a Krylov iterative solver. If however a naive implementation ( $\mathcal{O}(N^2)$ ) were to be used, a matrix–vector product would cost  $\mathcal{O}(10^{12})$  flops, an exorbitant number of computations indeed, even on a large cluster. In this sense, such scaling does not merely accelerate the computation of the solution, it makes possible the actual treatment of such problems.

**Table 2**  
Parameters for timing experiments.

	Volume ratio ( $\phi$ )	Speed of sound ( $c$ )	Density ( $\rho$ )	Radius ( $r$ )
1	0.01	0.2	0.5	0.005
2	0.1	0.2	0.5	0.005
3	0.01	6	8	0.6
4	0.1	6	8	0.6

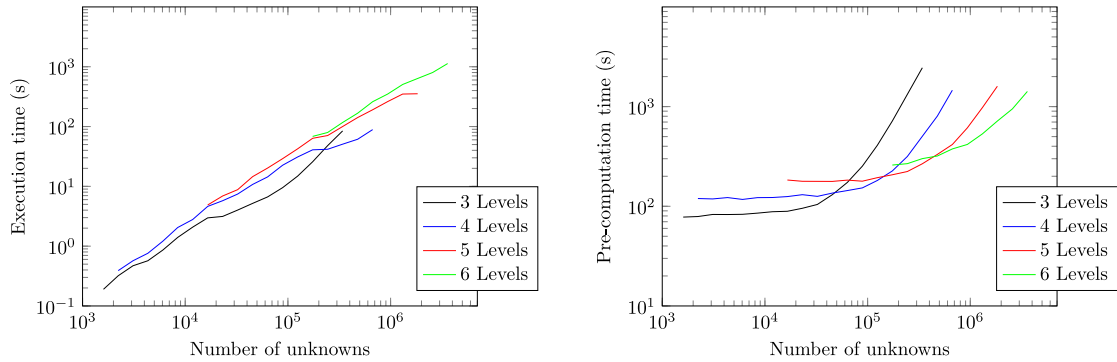


**Fig. 7.** Timing example—volume ratio:  $\phi = 0.01$ , scatterer speed of sound:  $c = 0.2$ , scatterer density:  $\rho = 0.5$ , scatterer radius:  $r = 0.005$ . Left: execution time (s) for matrix–vector product. Right: pre-computation time (s). Target accuracy  $\varepsilon = 10^{-7}$ .

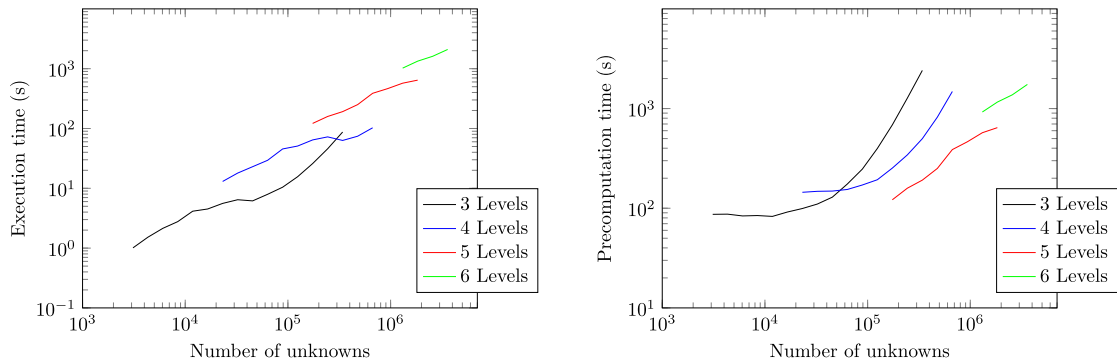


**Fig. 8.** Timing example—volume ratio:  $\phi = 0.1$ , scatterer speed of sound:  $c = 0.2$ , scatterer density:  $\rho = 0.5$ , scatterer radius:  $r = 0.005$ . Left: execution time (s) for matrix–vector product. Right: pre-computation time (s). Target accuracy  $\varepsilon = 10^{-7}$ .

For demonstration purposes, four different experiments were carried out as follows: in each case,  $N$  scatterers of radius  $r$ , speed of sound  $c$  and density  $\rho$  were located uniformly at random in a cube in such a way that the volume ratio occupied by the scatterers remained constant and equal to  $\phi$  (see Table 2). Then, the tree was built using various number of levels and a single application of the fast matrix–vector product was performed (with precision parameter  $\varepsilon = 10^{-7}$ ). Both operations were timed.

The timing results are shown in Figs. 7–10 on log–log plots. The left plots show the execution time for the matrix–vector product whereas the right plots show the pre-computation time. The first thing to be noticed is that by choosing the appropriate number of levels, it is indeed possible to achieve linear computation time (as a function of the number of unknowns) as claimed earlier. Another important thing to notice is that it seems generally more expensive to apply the operator  $TA$  with small scatterers than with larger one. This is because small scatterers are usually associated with problems in the low-frequency regime and are more expensive to handle due to the nature of the translation operators used there (larger algorithmic constant). We also notice some sort of “kink” in the execution time of Figs. 7–8. These occur when a level goes from low-frequency to high-frequency: as we increase the number of scatterers, the size of each box at each level increases. When such size goes from being smaller than a wavelength to being larger, the algorithm switches from using dense translation operators to diagonal ones. This results in a slight decrease in computational time despite the fact that the problem is larger. As for the pre-computation time, for a fixed number of levels, it goes from being roughly constant to  $\mathcal{O}(N^2)$  as we increase the number of unknowns. This is because when too few levels are being used, the work is mostly located in the close-term interactions of which there are  $\mathcal{O}(N^2)$ . Finally, it should be said that the running time is greatly satisfactory. Indeed, we see that in all cases less than roughly three minutes are needed to perform a single matrix–vector product for problems containing approximately  $10^6$  unknowns, and this is adequate for most purposes.

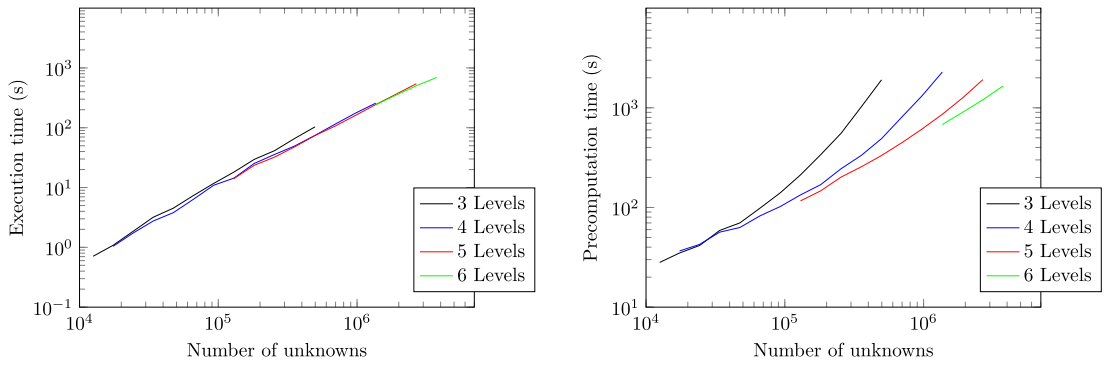


**Fig. 9.** Timing example—volume ratio:  $\phi = 0.01$ , scatterer speed of sound:  $c = 6$ , scatterer density:  $\rho = 8$ , scatterer radius:  $r = 0.6$ . Left: execution time (s) for matrix–vector product. Right: pre-computation time (s). Target accuracy  $\varepsilon = 10^{-7}$ .

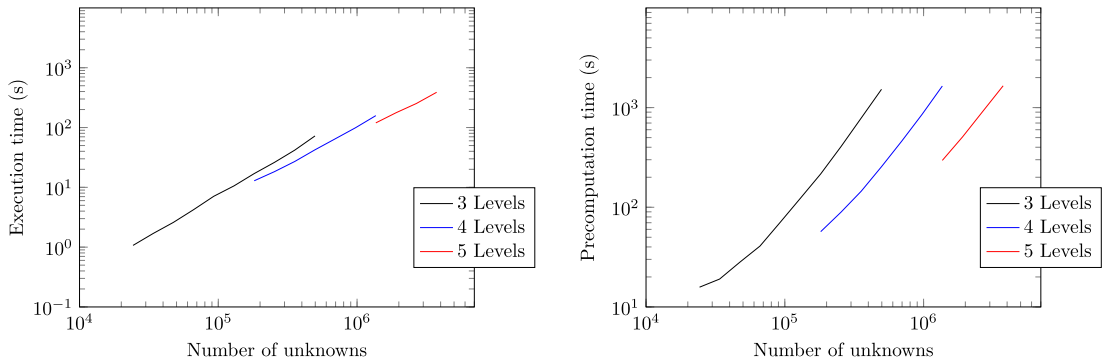


**Fig. 10.** Timing example—volume ratio:  $\phi = 0.1$ , scatterer speed of sound:  $c = 6$ , scatterer density:  $\rho = 8$ , scatterer radius:  $r = 0.6$ . Top: execution time (s) for matrix–vector product. Bottom: pre-computation time (s) for up to 5 levels. Target accuracy  $\varepsilon = 10^{-7}$ .

### 3. A numerical study of super-resolution in highly-heterogeneous 3D media

In this section, we numerically study the phenomenon of super-resolution as described in [25–27]. Briefly, super-resolution means that it is possible to obtain wave refocusing *beyond the diffraction limit* in the context of a *time-reversal experiment* through the *addition of small, strong scatterers in the vicinity of a point source*.

We shall first describe the nature of a time-reversal experiment as well as its behavior in a homogeneous medium. Then, we will provide numerical examples where super-resolution is indeed observed. Finally, we shall compare our results with those expected from homogenization theory and show that they are in excellent agreement.

#### 3.1. Numerical observation of super-resolution

We begin with the numerical observation of super-resolution phenomena in the context of a time-reversal experiment. For this purpose, we first recall the nature of a time-reversal experiment in a homogeneous medium: a point source located somewhere within some medium emits a short pulse and the total field generated is recorded at receivers located on some sampling manifold (generally a spherical shell in the far-field of both the source and the scatterers). The recorded signals are then time-reversed (conjugated in Fourier space) and sent back into the medium. In appropriate circumstances, the time-reversed waves will refocus at the original location of the source.

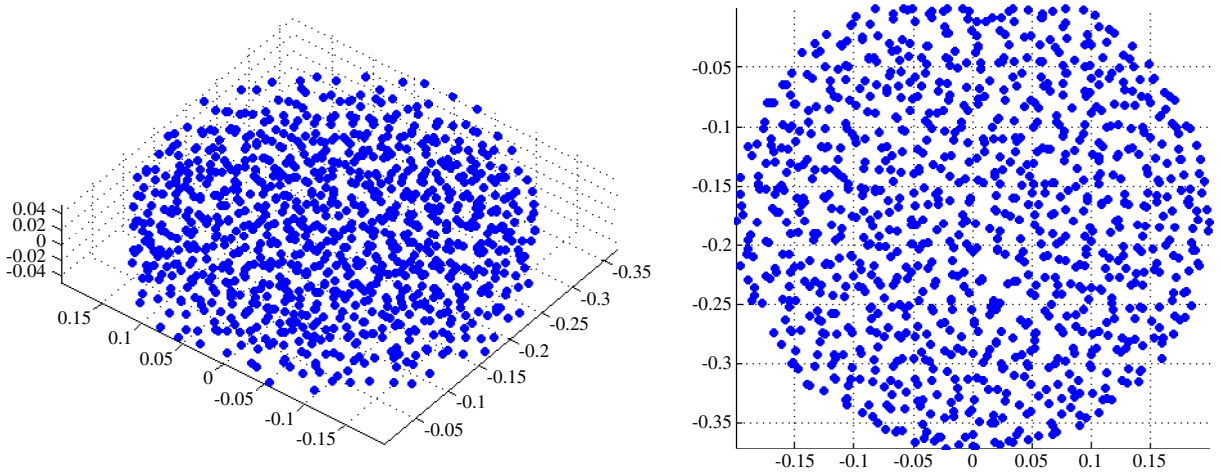
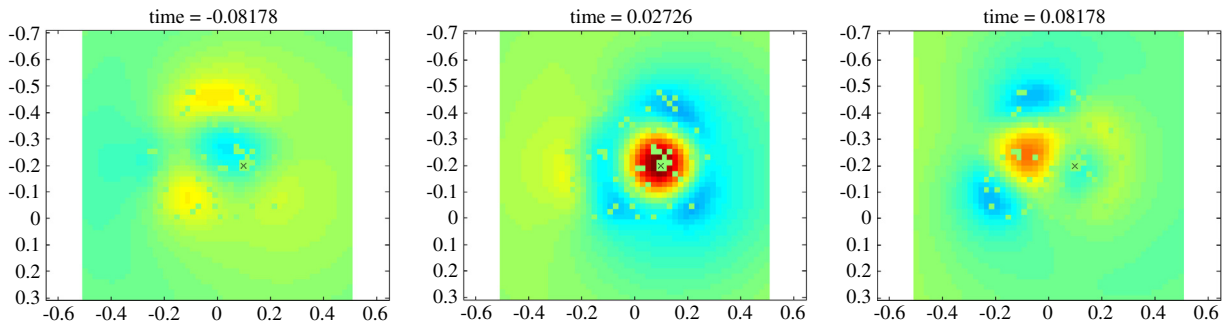
In this light, and using the aforementioned algorithm, we proceed to the following simulations: small, strong penetrable spheres distributed uniformly at random (without touching) within a region having the shape of a *truncated cylinder* as shown in Fig. 11, in the vicinity a source location. Then, we carried out time-reversal experiments as just described (the particular shape is similar to an ergodic cavity and was chosen in order to increase scattering in the homogenized truncated cylinder). We tried different combinations of parameters as shown in Table 3.  $N$  represents the number of scatterers,  $r$  their radii,  $c$  and  $\rho$  their internal speed of sound and density respectively, whereas  $R$  represents the radius of the cluster,  $t$  its thickness and  $\zeta$  the distance from the center to the planar surface.

The pressure field of the time-reversed signal is shown in Figs. 12–15 around time  $t = 0$ . In each case, the wavelength of the carrier frequency is  $\lambda_0 = 1$  which implies a resolution limit of approximately  $\approx \frac{\lambda_0}{2} = 0.5$ . What is noticed again here is a *spatio-temporal focusing* of the time-reversed signal; the energy concentrates close to the original location of the source at a particular instance in time. Moreover, it is to be noted that in all three cases the diffraction limit in homogeneous media

**Table 3**

Properties of truncated cylindrical clusters and their scatterers.

Sim.	Cluster radius ( $R$ )	offset ( $\zeta$ )	Thickness ( $t$ )	# ( $N$ )	Radius ( $r$ )	Speed ( $c$ )	Density ( $\rho$ )
1	$0.3\lambda_0$	$0.2\lambda_0$	$0.06\lambda_0$	6000	$0.005\lambda_0$	$0.1c_0$	$\rho_0$
2	$0.3\lambda_0$	$0.2\lambda_0$	$0.06\lambda_0$	6000	$0.005\lambda_0$	$0.1c_0$	$\rho_0$
3	$0.3\lambda_0$	$0.2\lambda_0$	$0.05\lambda_0$	5000	$0.005\lambda_0$	$0.1c_0$	$0.2\rho_0$
4	$0.175\lambda_0$	$0.125\lambda_0$	$0.05\lambda_0$	5000	$0.0035\lambda_0$	$0.021c_0$	$0.2\rho_0$

**Fig. 11.** Example of a cluster of small, strong scatterers within a region having the form of a truncated cylinder. Left: side view, Right: top view.**Fig. 12.** Time-reversed pressure field in  $x$ - $y$  plane for a point source in a truncated cylinder. Source located at:  $(0.1, -0.2, 0)\lambda_0$ ,  $\sigma = 0.15$ ; Dimensions of cluster:  $R = 0.3\lambda_0$ ,  $d = 0.2\lambda_0$ ,  $t = 0.06\lambda_0$ ; Properties of small scatterers:  $N = 6000$ ,  $r = 0.005\lambda_0$ ,  $\rho = \rho_0$ ,  $c = 0.1c_0$ ; Effective properties:  $\rho_{\text{eff}} = \rho_0$ ,  $c_{\text{eff}} = 0.2545c_0$ . Left:  $t = -0.082$ , Middle:  $t = 0.027$ , Right:  $t = 0.082$ .

is beaten; in Figs. 12 and 13, a resolution of approximately  $\frac{\lambda_0}{20}$  is achieved whereas a resolution beyond  $\frac{\lambda_0}{80}$  is achieved in Figs. 14 and 15.

The size of the focal spot depends on the properties of the scatterers constituting the cluster; the lower their speed of sound, the smaller the spot. As will be explained in the following sections, the size of the spot appears to reach the resolution limit in some *effective medium*. Another interesting point to be noted is that in Fig. 15, where even the cluster itself has dimensions smaller than the resolution limit. Yet, super-resolution is still achieved. This is somewhat surprising since the field at the boundary cannot be resolved through time-reversal.

In short, these numerical examples demonstrate that it is indeed possible to beat the diffraction limit through the addition of small, strong scatterers in the vicinity of a source in the context of a time-reversal experiment. We note that, to the authors' knowledge, this is the first time such numerical simulations have been performed for such a large problem of this type. As explained in the introduction, it was previously not possible to solve such problem from a computational standpoint, and it is only the introduction of our wideband 3D algorithm that brought such a feat within reach.

### 3.2. Super-resolution and effective medium theory

In this section, we would like to verify whether it is possible to explain the phenomena observed in the previous section through Effective Medium Theory (EMT). That is, we would like to numerically investigate whether it is possible that, under

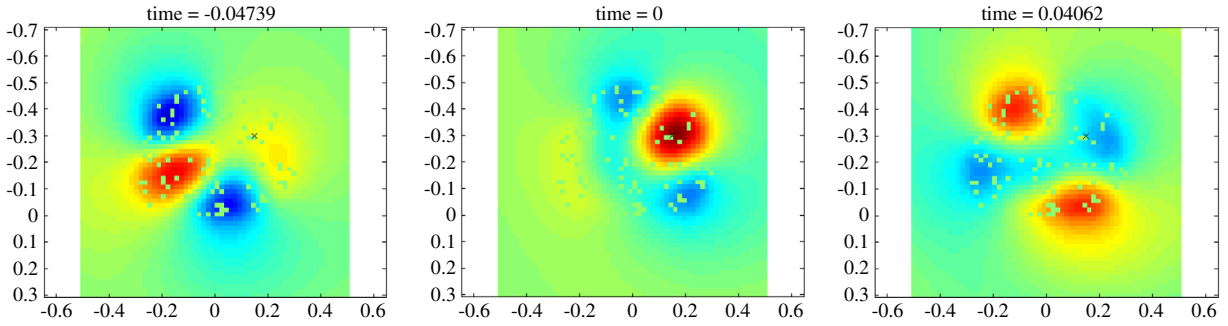


**Fig. 13.** Time-reversed pressure field in  $x$ - $y$  plane for a point source in an ergodic cylinder. Source located at:  $(0.15, -0.3, 0.)\lambda_0$ ,  $\sigma = 0.15$ ; Dimensions of cluster:  $R = 0.3\lambda_0$ ,  $d = 0.2\lambda_0$ ,  $t = 0.06\lambda_0$ ; Properties of small scatterers:  $N = 6000$ ,  $r = 0.005\lambda_0$ ,  $\rho = \rho_0$ ,  $c = 0.1c_0$ ; Effective properties:  $\rho_{\text{eff}} = \rho_0$ ,  $c_{\text{eff}} = 0.2545c_0$ . Left:  $t = -0.047$ , Middle:  $t = 0$ , Right:  $t = 0.041$ .

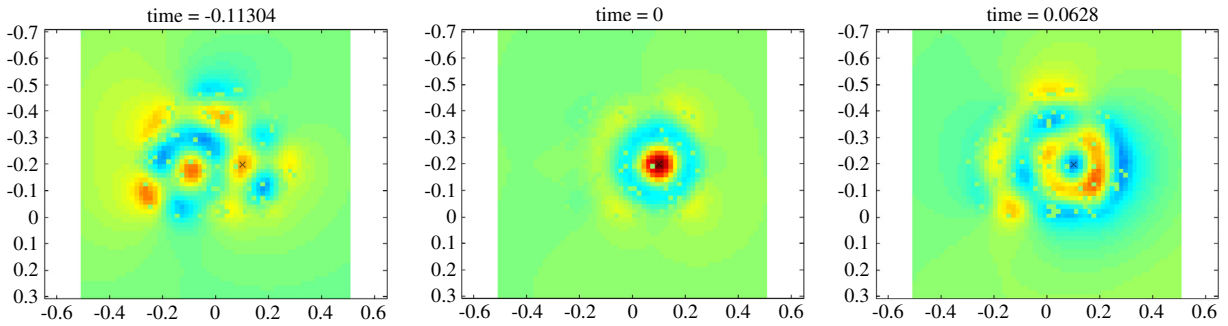


**Fig. 14.** Time-reversed pressure field in  $x$ - $y$  plane for a point source in an ergodic cylinder. Source located at:  $(0.1, -0.2, 0.)\lambda_0$ ,  $\sigma = 0.15$ ; Dimensions of cluster:  $R = 0.3\lambda_0$ ,  $d = 0.2\lambda_0$ ,  $t = 0.05\lambda_0$ ; Properties of small scatterers:  $N = 5000$ ,  $r = 0.005\lambda_0$ ,  $\rho = 0.2\rho_0$ ,  $c = 0.1c_0$ ; Effective properties:  $\rho_{\text{eff}} = 0.8109\rho_0$ ,  $c_{\text{eff}} = 0.1487c_0$ . Left:  $t = -0.113$ , Middle:  $t = 0$ , Right:  $t = 0.063$ .

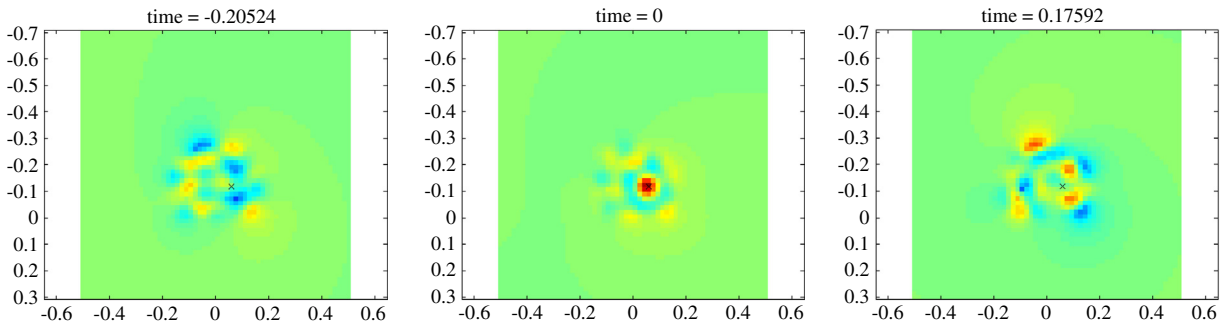


**Fig. 15.** Time-reversed pressure field in  $x$ - $y$  plane for a point source in an ergodic cylinder. Source located at:  $(0.058\bar{3}, -0.11\bar{6}, 0.)\lambda_0$ ,  $\sigma = 0.15$ ; Dimensions of cluster:  $R = 0.175\lambda_0$ ,  $d = 0.125\lambda_0$ ,  $t = 0.05\lambda_0$ ; Properties of small scatterers:  $N = 5000$ ,  $r = 0.0035\lambda_0$ ,  $\rho = 0.2\rho_0$ ,  $c = 0.021c_0$ ; Effective properties:  $\rho_{\text{eff}} = 0.8197\rho_0$ ,  $c_{\text{eff}} = 0.03c_0$ . Left:  $t = -0.205$ , Middle:  $t = 0$ , Right:  $t = 0.176$ .

certain circumstances, a cluster of strong scatterers whose radii are smaller than the wavelength of the signal emitted by a source, could in fact behave as a homogeneous body, and whether an apparent super-resolution phenomenon can be observed in this case.

For this purpose, we considered a cluster having the shape of a *truncated sphere* as shown in Fig. 16. The reason we chose such a shape is to simplify the pre-computations of the T-matrix of the homogenized body, and the reason why we truncated it is to increase scattering and avoid some of the degenerate modes associated with a sphere. The scatterers are located on a periodic lattice which has been perturbed through a small random quantity. We note that in the previous section, the scatterers were randomly distributed. Here we demonstrate that super-resolution is also observed in the case of a perturbed lattice, as well as studying its link to EMT.

An important point must be mentioned before moving further: due to the way the T-matrix method is formulated, the SWF expansions introduced in Section 2.1 are only valid either *inside* (RSWF expansion) a scatterer or *outside the smallest sphere* containing the scatterer (ISWF expansion). This limitation leaves a region between the boundary and the circumscribing homogenized sphere (Fig. 18, bottom right), in which ISWF cannot generally be used to represent the field.

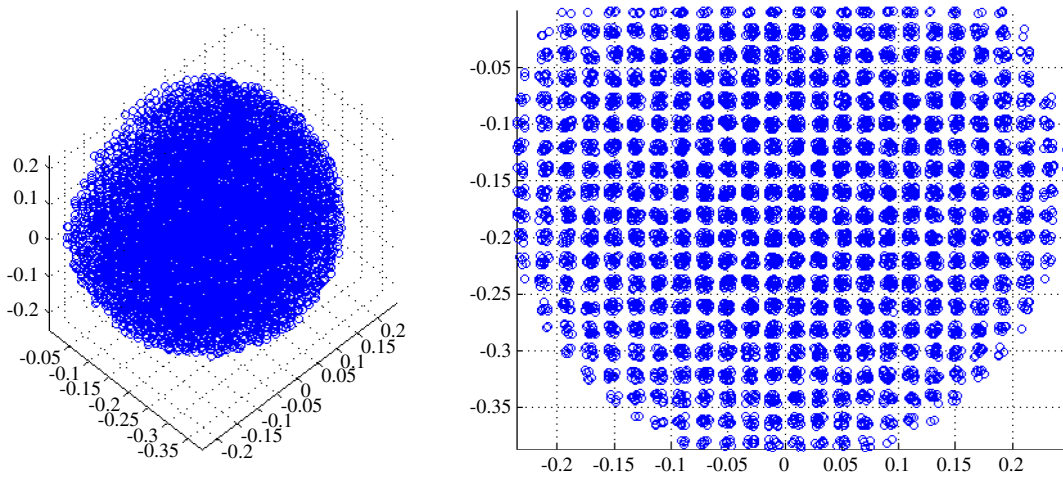


Fig. 16. Example of a cluster of small, strong scatterers within a region having the form of a truncated cylinder. Left: side view, Right: top view.

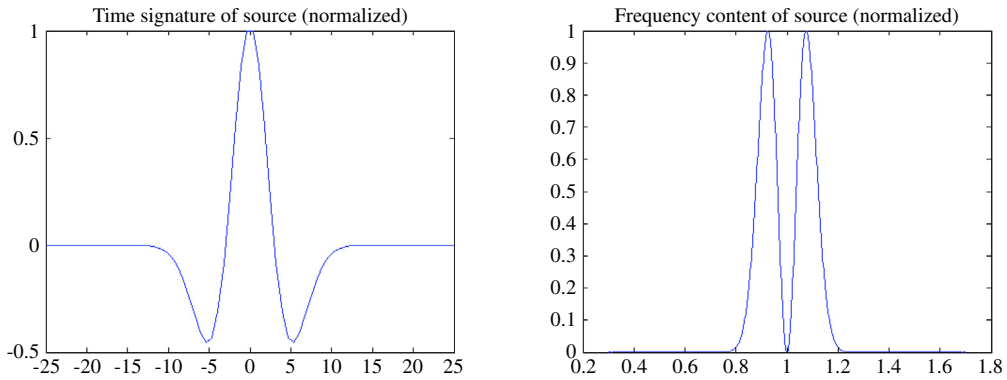


Fig. 17. Ricker wavelet. Left: time domain, Right: frequency domain.

This is known as the *Rayleigh hypothesis* (see e.g. [54, Section 5.1]—T-matrix Ansatz). In the results that follow, we generally plot the field in this region for aesthetics. However, the values of the field there should not be considered reliable.

We numerically study the behavior of various clusters of strong, small scatterers in the context of a time-reversal experiment when the source emits a *broadband signal*. The signal takes the form of a Ricker wavelet (Mexican hat; Fig. 17), i.e.,

$$f(t) = \frac{2}{\sqrt{3\sigma\pi^{1/4}}} \left( 1 - \frac{t^2}{\sigma^2} \right) e^{-\frac{t^2}{2\sigma^2}}.$$

The experiments are carried out as follows: three different clusters containing {1826, 3618, 17 872} spherical scatterers of radius {0.008, 0.005, 0.0038} respectively arranged on randomly perturbed lattices are generated. For each cluster, the scatterer properties and volume density were chosen in such a way that *effective* density and speed of sound ( $c_{\text{eff}} = 0.2902c_0$ ,  $\rho_{\text{eff}} = \rho_0$ ), as dictated by effective medium theory in the Maxwell–Garnett approximation described for instance in [68]

Eqs. (1)–(2),  $\frac{\rho_{\text{eff}} - \rho_0}{2\rho_{\text{eff}} + \rho_0} = p \frac{\rho_s - \rho_0}{2\rho_s + \rho_0}$ ,  $\kappa_{\text{eff}} = \left( \frac{p}{\kappa_s} + \frac{1-p}{\kappa_0} \right)^{-1}$ , and  $c_{\text{eff}}^2 = \frac{\kappa_{\text{eff}}}{\rho_{\text{eff}}}$ , where the subscript  $s$  indicates scatterer properties, the subscript  $0$  indicates background properties,  $\rho$  is the density,  $\kappa$  is the bulk modulus and  $p$  is the volume ratio occupied by the scatterers) are all the same. A fourth experiment was also carried out with a homogeneous (homogenized) inclusion having the same shape as the cluster, and with its properties equal to the effective properties just mentioned.

The results are shown in Fig. 18 where we plotted the pressure field of the time-reversed signal at time  $t = 0$ . What is seen there is a very good agreement in all cases. These interesting results lead to two main conclusions: first, it appears that in all cases involving small scatterers, we are indeed in the EMT regime [68]. This is not too surprising for among all examples, the smallest wavelength contained in the signal is at least 37 times larger than the diameter of the scatterers and the smallest *effective* wavelength within the cluster is approximately 11 times larger than that same quantity. The second conclusion is that it appears that it is indeed possible to achieve an apparent super-resolution with a mere homogeneous body. Of course in real-life applications it is most likely more advantageous to use a composite rather than a homogeneous body since the former offers a much wider range of effective physical properties. On the other hand, it is theoretically much simpler to deal with a homogeneous body than with a cluster and this offers great leverage.

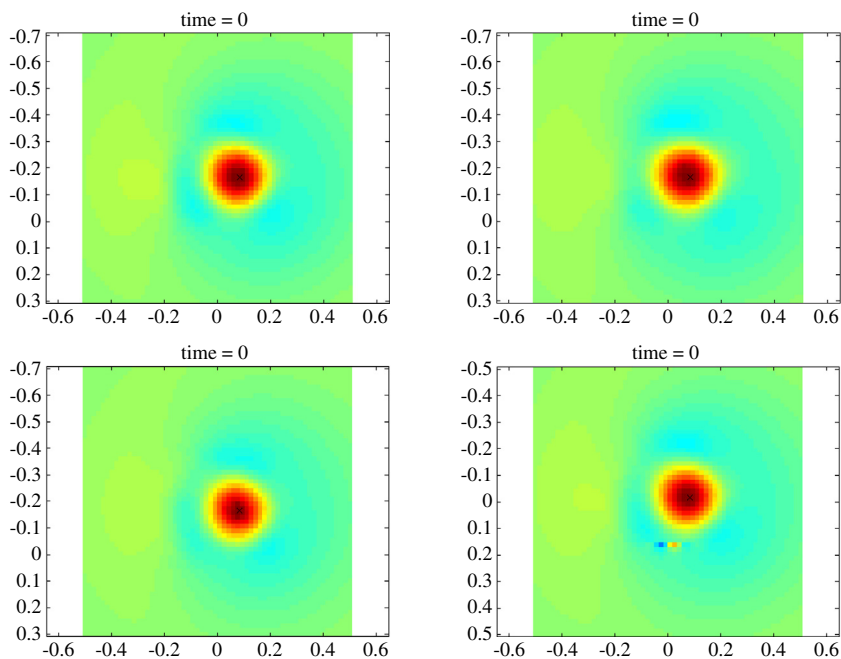


**Fig. 18.** Time-reversed field from a point source located at  $(0.08\bar{3}, -0.1\bar{6}, 0)$  emitting a Ricker wavelet ( $\sigma = 0.7$ ) in a spheroid cavity of radius  $R = 0.25$  and offset  $\zeta = 0.15$  and having effective properties  $c_{\text{eff}} = 0.292 c_0$  and  $\rho_{\text{eff}} = 1 \rho_0$ . From Top to bottom, Left to right: number of scatterers  $N = \{17872, 3618, 1826, \text{Homogeneous}\}$ , radius of scatterers  $r = \{0.0038, 0.005, 0.008\} \lambda_0$ .

#### 4. Conclusion

In conclusion, we have introduced a wideband fast algorithm capable of simulating the propagation of time-harmonic acoustic waves through clusters containing many strong and penetrable scatterers in three dimensions. The algorithm is fast in the sense that it scales linearly with the number of unknowns, and does not suffer from any breakdown at low or high frequencies. We have also bolstered our claims through multiple numerical examples which demonstrate the algorithmic complexity of the method. Finally, we used our algorithm to study the phenomenon of super-resolution in time-reversal refocusing in the presence of small strong scatterers around the source. We showed that super-resolution can indeed be observed in this case, and that it can be explained through homogenization theory in the sense that the radius of the time-reversed focal spot is equal to half the effective wavelength. These numerical findings confirm and illustrate the theoretical predictions found in the literature, using both periodic and random homogenization [28,29]. This interpretation is sufficient and holds in many physical situations, when the conditions of homogenization are met, which means, when the typical scale of variation of the scattering medium is smaller than the effective wavelength. Very recently, time reversal in a sub-wavelength-scaled resonant medium, namely a system of Helmholtz resonators in the quasi-stationary regime, was mathematically analyzed [69], which goes beyond the homogenization regime addressed in our paper.

#### References

- [1] K. Aydin, I. Bulu, E. Ozbay, Subwavelength resolution with a negative-index metamaterial superlens, *Appl. Phys. Lett.* 90 (2007) 254102.
- [2] M. Ambati, N. Fang, C. Sun, X. Zhang, Surface resonant states and superlensing in acoustic metamaterials, *Phys. Rev. B* 75 (2007) 195447.
- [3] J. Li, L. Fok, X. Yin, G. Bartal, X. Zhang, Experimental demonstration of an acoustic magnifying hyperlens, *Nature Mater.* 8 (2009) 931–934.
- [4] I.M. Vellekoop, A.P. Mosk, Universal optimal transmission of light through disordered materials, *Phys. Rev. Lett.* 101 (2008) 120601.
- [5] Z. Jaksic, N. Dalarsson, M. Maksimovic, Negative refractive index metamaterials: Principles and applications, *Micro. Rev.* (2006) 36–49.
- [6] J.B. Pendry, J. Li, An acoustic metafluid: realizing a broadband acoustic cloak, *New J. Phys.* 10 (2008).
- [7] S. Zhang, C. Xia, N. Fang, Broadband acoustic cloak for ultrasound waves, *Phys. Rev. Lett.* 106 (2) (2011) 24301.
- [8] X. Zhang, Z. Liu, Superlenses to overcome the diffraction limit, *Nature Mater.* 7 (2008) 435–441.
- [9] M. Fink, Time reversal of ultrasonic fields. I. Basic principles, *IEEE Trans. Ultrason. Ferroelectr. Freq. Control* 39 (1992) 555–566.
- [10] M. Fink, Time reversed acoustics, *Sci. Am.* 281 (1999) 91–97.
- [11] M. Fink, D. Cassereau, A. Derode, C. Prada, P. Roux, M. Tanter, J.-L. Thomas, F. Wu, *Rep. Progr. Phys.* 63 (2000) 1933–1995.
- [12] L. Borcea, G. Papanicolaou, C. Tsogka, J. Berryman, Imaging and time reversal in random media, *Inverse Problems* 18 (2002) 1247–1279.
- [13] J. de Rosny, G. Lerosey, M. Fink, Theory of electromagnetic time-reversal mirrors, *IEEE Trans. Antennas and Propagation* 58 (2010) 3139–3149.
- [14] D. Cassereau, F. Fink, Time reversal of ultrasonic fields - part III: Theory of the closed time-reversal cavity, *IEEE Trans. Ultrason. Ferroelectr. Freq. Control* 39 (1992) 579–592.
- [15] W. Elmore, M. Heald, *Physics of Waves*, Dover, 1969.
- [16] P. Blomgren, G. Papanicolaou, H. Zhao, Super-resolution in time-reversal acoustics, *J. Acoust. Soc. Am.* 111 (2002) 230–248.
- [17] A. Derode, A. Tourin, J. de Rosny, M. Tanter, S. Yon, M. Fink, Taking advantage of multiple scattering to communicate with time-reversal antennas, *Phys. Rev. Lett.* 90 (2003) 014301.

- [18] J. de Rosny, A. Tourin, A. Derode, B. van Tiggelen, M. Fink, Relation between time reversal focusing and coherent backscattering in multiple scattering media: A diagrammatic approach, *Phys. Rev. E* 70 (2004) 046601.
- [19] J.-P. Fouque, J. Garnier, A. Nachbin, K. Solna, Time reversal refocusing for point source in randomly layered media, *Wave Motion* 42 (2005) 238–260.
- [20] J.-P. Fouque, J. Garnier, K. Solna, Time reversal super resolution in randomly layered media, *Wave Motion* 43 (2006) 646–666.
- [21] J.-P. Fouque, J. Garnier, G. Papanicolaou, K. Solna, *Wave Propagation and Time Reversal in Randomly Layered Media*, Springer, 2007.
- [22] J. de Rosny, M. Fink, Overcoming the diffraction limit in wave physics using a time-reversal mirror and a novel acoustic sink, *Phys. Rev. Lett.* 89 (2002) 124301.
- [23] J. de Rosny, M. Fink, Focusing properties of near-field time reversal, *Phys. Rev. A* 76 (2007) 065801.
- [24] G. Lerosey, J. de Rosny, A. Tourin, M. Fink, Focusing beyond the diffraction limit with far-field time reversal, *Science* 315 (2007) 1120.
- [25] F. Lemoult, M. Fink, G. Lerosey, Acoustic resonators for far-field control of sound on a subwavelength scale, *Phys. Rev. Lett.* 107 (2011) 064301.
- [26] G. Lerosey, F. Lemoult, M. Fink, Acoustic resonators for far field control of sound on a subwavelength scale, in: *META'12*, 2011.
- [27] F. Lemoult, M. Fink, G. Lerosey, Dispersion in media containing resonant inclusions: where does it come from? in: 2012 Conference on Lasers and Electro-Optics, (CLEO), IEEE, 2012, pp. 1–2.
- [28] H. Ammari, E. Bonnetier, Y. Capdeboscq, Enhanced resolution in structured media, *SIAM J. Appl. Math.* 70 (2009) 1428–1452.
- [29] C. Gomez, Time-reversal superresolution in random waveguides, *SIAM Multiscale Model. Simul.* 7 (2009) 1348–1386.
- [30] H.W. Cheng, W.Y. Crutchfield, Z. Gimbutas, L.F. Greengard, J.F. Ethridge, J. Huang, V. Rokhlin, N. Yarvin, J. Zhao, A wideband fast multipole method for the helmholtz equation in three dimensions, *J. Comput. Phys.* 216 (2006) 300–325.
- [31] N.A. Gumerov, R. Duraiswami, Computation of scattering from N spheres using multipole reexpansion, *J. Acoust. Soc. Am.* 112 (2002) 2688–2701. <http://dx.doi.org/10.1121/1.1517253>.
- [32] A. Hesford, J.P. Astheimer, L. Greengard, R. Wang, A mesh-free approach to acoustic scattering from multiple spheres nested inside a large sphere using diagonal translation operators, *J. Acoust. Soc. Am.* 127 (2) (2010) 850–861.
- [33] S. Koc, W.C. Chew, Calculation of acoustical scattering from a cluster of scatterers, *J. Acoust. Soc. Am.* 103 (2) (1998).
- [34] P.C. Waterman, New formulation of acoustic scattering, *J. Acoust. Soc. Am.* 45 (6) (1969) 1417–1429.
- [35] X. Ao, C.T. Chan, Far-field image magnification for acoustic waves using anisotropic acoustic metamaterials, *Phys. Rev. E* 77 (2008) 25601.
- [36] M. Kafesaki, E.N. Economou, Multiple-scattering theory for the three-dimensional periodic acoustic composites, *Phys. Rev. B* 60 (17) (1999) 11993.
- [37] P.A. Martin, *Multiple Scattering: Interaction of Time-harmonic Waves with N Obstacles*, Cambridge University Press, 2006.
- [38] V. Rokhlin, Rapid solution of integral equations of classical potential theory, *J. Comput. Phys.* 60 (1983) 187–207.
- [39] L. Greengard, V. Rokhlin, A fast algorithm for particle simulations, *J. Comput. Phys.* 135 (1987) 280–292.
- [40] L. Greengard, J. Huang, V. Rokhlin, S. Wandzura, Accelerating fast multipole methods for the Helmholtz equation at low frequencies, *IEEE Comput. Sci. Eng.* 5 (3) (1998) 32–38.
- [41] L. Greengard, V. Rokhlin, A new version of the fast multipole method for the Laplace equation in three dimensions, *Acta Numer.* 6 (2008) 229–269.
- [42] C. Cecka, E. Darve, Fourier-based fast multipole method for the Helmholtz equation, *SIAM J. Sci. Comput.* 35 (2013) 79–103.
- [43] A. Aubry, A. Derode, Detection and imaging in a random medium: A matrix method to overcome multiple scattering and aberration, *J. Appl. Phys.* 106 (2009) 044903.
- [44] F. Lemoult, G. Lerosey, J. de Rosny, M. Fink, Resonant metalenses for breaking the diffraction barrier, *Phys. Rev. Lett.* 104 (2010) 203901.
- [45] F. Lemoult, A. Ourir, J. de Rosny, A. Tourin, M. Fink, G. Lerosey, Time reversal in subwavelength-scaled resonant media: Beating the diffraction limit, *Int. J. Microw. Sci. Tech.* 2011 (2011) 425710.
- [46] N.A. Gumerov, R. Duraiswami, Computation of scattering from clusters of spheres using the fast multipole method, *J. Acoust. Soc. Am.* 117 (4) (2005) 1744–1761.
- [47] P.-D. Létourneau, *Fast algorithms and imaging in strongly-scattering media* (Ph.D. thesis), Stanford University, 2013, <https://purl.stanford.edu/pf259md7940>.
- [48] M. Abramowitz, I.A. Stegun, *Handbook of Mathematical Functions*, tenth ed., National Bureau of Standards, 1972.
- [49] D. Colton, R. Kress, *Inverse Acoustic and Electromagnetic Scattering Theory*, second ed., Springer, 1998.
- [50] R. Kress, G.F. Roach, Transmission problems for the Helmholtz equation, *J. Math. Phys.* 19 (1978) 1433–1437.
- [51] R. Kress, G.F. Roach, On mixed boundary value problems for the Helmholtz equation, *Proc. Roy. Soc. Edinburgh Sect. A* 77 (1977) 65–77.
- [52] M.I. Mischenko, G. Videen, V.A. Babenko, N.G. Khlebtsov, T. Wriedt, T-matrix theory of electromagnetic scattering by particles and its applications: a comprehensive reference database, *J. Quant. Spectrosc. Radiat. Transfer* 88 (2004) 357–406.
- [53] M. Born, E. Wolf, *Principles of Optics*, seventh ed., Cambridge University Press, 1999.
- [54] M.I. Mischenko, L.D. Travis, A.A. Lasis, *Scattering, Absorption and Emission of Light by Small Particles*, third ed., Cambridge University press, 2002.
- [55] V.V. Varadan, V.K. Varadan, Configurations with finite numbers of scatterers – a self-consistent t-matrix approach, *J. Acoust. Soc. Amer.* 70 (1981) 213–217.
- [56] A Succinct Way to Diagonalize the Translation Matrix in Three Dimensions, in: *Ant. and Prop. Soc. Int. Symp.*, vol. 3, 1997.
- [57] S. Koc, J.M. Song, W.C. Chew, Error analysis for the numerical evaluation of the diagonal forms of the scalar spherical addition theorem, *SIAM J. Numer. Anal.* 36 (3) (1999) 906–921.
- [58] V. Rokhlin, Diagonal forms of translation operators for the Helmholtz equation in three dimensions. Technical report, Yale University, 1992.
- [59] E. Darve, The fast multipole method I: Error analysis and asymptotic complexity, *SIAM J. Numer. Anal.* 38 (1) (2001) 98–128.
- [60] M.A. Epton, D. Dembart, Multipole translation theory for the three-dimensional Laplace and Helmholtz equations, *SIAM J. Sci. Comput.* 16 (4) (1995) 865–897.
- [61] E. Wigner, *Gruppentheorie und ihre Anwendung auf die Quanten-mechanik der Atomspektren*, Vieweg, Wies-baden, Germany, 1931.
- [62] A.R. Edmonds, *Angular Momentum in Quantum Mechanics*, third ed., Princeton University press, 1974.
- [63] C.H. Choi, J. Ivanic, M.S. Gordon, K. Ruedenberg, Rapid and stable determination of rotation matrices between spherical harmonics by direct recursion, *J. Chem. Phys.* 111 (19) (1999) 8825.
- [64] N.A. Gumerov, R. Duraiswami, Fast, exact, and stable computation of multipole translation and rotation coefficients for the 3-d Helmholtz equation. Technical report, University of Maryland, 2001.
- [65] E. Darve, The fast multipole method: Numerical implementation, *J. Comput. Phys.* 160 (2000) 195240.
- [66] L. Ying, G. Biros, D. Zorin, A kernel-independent adaptive fast multipole method algorithm in two and three dimensions, *J. Comput. Phys.* 196 (2004) 591–626.
- [67] I. Umberto, V. Marchese, *Acoustic Simulation TOol (Acousto)*, Version 1.3-beta, January 2011. <http://acousto.sourceforge.net/index.php>.
- [68] J. Mei, Z. Liu, W. Wen, P. Sheng, Effective mass density of fluid-solid composites, *Phys. Rev. Lett.* 96 (2) (2006) 024301.
- [69] H. Ammari, H. Zhang, A mathematical theory of super-resolution by using a system of sub-wavelength Helmholtz resonators, *Comm. Math. Phys.* 337 (2015) 379–428.